Lithos 310–311 (2018) 269–287

Contents lists available at ScienceDirect

Lithos

journal homepage: www.elsevier.com/locate/lithos

Tectonic slicing and mixing processes along the subduction interface: The Sistan example (Eastern Iran)

G. Bonnet [a,*], P. Agard [a,b], S. Angiboust [c], P. Monié [d], M. Jentzer [a], J. Omrani [e], H. Whitechurch [f], M. Fournier [a]

[a] Sorbonne Université, CNRS-INSU, Institut des Sciences de la Terre de Paris, ISTeP UMR 7193, F-75005 Paris, France
[b] Institut Universitaire de France, F-75005 Paris, France
[c] Institut de Physique du Globe de Paris, Sorbonne Paris Cité, Univ. Paris Diderot, CNRS, F-75005 Paris, France
[d] Géosciences Montpellier UMR-CNRS 5243, Place E. Bataillon, 34090 Montpellier, France
[e] Geological Survey of Iran, Tehran, Iran
[f] Institut de Physique du Globe de Strasbourg, EOST-CNRS-UMR 7516, Université de Strasbourg, 67000 Strasbourg, France

ARTICLE INFO

Article history:
Received 31 October 2017
Accepted 17 April 2018
Available online 22 April 2018

Keywords:
Sistan ocean
Iran
Lawsonite eclogite
Blueschist
Thermodynamic modeling
Ar–Ar geochronology
Subduction plate interface
Mélange-forming processes

ABSTRACT

Suture zones preserve metamorphosed relicts of subducted ocean floor later exhumed along the plate interface that can provide critical insights on subduction zone processes. Mélange-like units are exceptionally well-exposed in the Sistan suture (Eastern Iran), which results from the closure of a branch of the Neotethys between the Lut and Afghan continental blocks. High pressure rocks found in the inner part of the suture zone (i.e., Ratuk complex) around Gazik are herein compared to previously studied outcrops along the belt. Detailed field investigations and mapping allow the distinction of two kinds of subduction-related block-in-matrix units: a siliciclastic-matrix complex and a serpentinite-matrix complex. The siliciclastic-matrix complex includes barely metamorphosed blocks of serpentinized peridotite, radiolarite and basalt of maximum greenschist-facies grade (i.e., maximum temperature of 340 °C). The serpentinite-matrix complex includes blocks of various grades and lithologies: mafic eclogites, amphibolitized blueschists, blue-amphibole-bearing metacherts and aegirine-augite-albite rocks. Eclogites reached peak pressure conditions around 530 °C and 2.3 GPa and isothermal retrogression down to 530 °C and 0.9 GPa. Estimation of peak PT conditions for the other rocks are less-well constrained but suggest equilibration at $P < 1$ GPa. Strikingly similar Ar–Ar ages of 86 ± 3 Ma, along ~70 km, are obtained for phengite and amphibole from fourteen eclogite and amphibolitized blueschist blocks. Ages in Gazik are usually younger than further south (e.g., Sulabest), but there is little age difference between the various kinds of rocks. These results (radiometric ages, observed structures and rock types) support a tectonic origin of the serpentinite-matrix mélange and shed light on subduction zone dynamics, particularly on coeval detachment and exhumation mechanisms of slab-derived rocks.

1. Introduction

Suture zones preserve metamorphosed relicts of subducted ocean floor later exhumed along the plate interface and provide critical insights on subduction zone processes (e.g., Agard et al., 2009; Guillot et al., 2009). Some preserve extensive subduction-related mélange-like units composed of a sedimentary or peridotite-derived matrix hosting blocks of variable size, metamorphic grade and nature (sediments, mafic or ultramafic material). Classic kilometer-scale mélange examples are found in California (Franciscan complex: Hsü, 1968; Tsujimori et al., 2007; Ukar and Cloos, 2013; Wakabayashi, 2015; Great Valley Group: Wakabayashi, 2017a; Santa Catalina Island: Bebout and Barton, 1993; Platt, 1975; Sorensen and Barton, 1987), in the Caribbean (Serpentinite mélange zone from Cuba/Dominican Republic/Guatemala/Nicaragua; Draper et al., 1991; Flores et al., 2013, 2015; Garcia-Casco et al., 2006; Goncalves et al., 2000; Harlow et al., 2004; Krebs et al., 2011; Martens et al., 2017; Martin et al., 2016; Tsujimori et al., 2006a), in Sulawesi (Parkinson, 1996), and m-hm scale zones are reported in the Western Alps (Angiboust et al., 2011; Federico et al., 2007) or in active subduction zones (Mariana forearc, Maekawa et al., 1995; Pabst et al., 2012). The main characteristics of these units are summed up in Table 1. Of particular interest is how these rocks may record processes such as slow vs fast exhumation, storage along the plate interface (in the "subduction channel") or thermal and chemical interactions with fluids and/or the mantle wedge above. By essence, however, mélange-like units are complex and may form from sedimentary, tectonic or diapiric mixing (Festa

* Corresponding author.
E-mail address: gbonnet01@gmail.com. (G. Bonnet).

https://doi.org/10.1016/j.lithos.2018.04.016
0024-4937/

Table 1
Synthesis of the variety of origins of serpentinite mélange-like units, structural thickness, diversity of metamorphism, block size, and metamorphic rinds from several examples in the world. PP = prehnite-pumpellyite, GS = greenschist, LB = lower blueschist, BS = blueschist, EC = eclogite, AM = amphibolite.

Mélange-like complexes	Origin	Structural thickness	Diversity of metamorphism						Size of blocks	Metasomatic rinds	References
			PP	GS	LB	BS	EC	AM			
Great Valley Group USA	Sedimentary	~1–2 km	x				x	x	cm to 500 m	Some	Wakabayashi (2017a)
Franciscan serpentinite mélanges USA	Disputed (tectonic or sedimentary)	<1.5 km	x			x	x	x	cm to 500 m	Some	Cloos (1982) Wakabayashi (2015)
Santa Catalina Serpentinite unit	Assumed tectonic	<1 km						x	~1 cm to ~1 km	Yes	Platt (1975) Sorensen and Barton (1987) Bebout and Barton (1993)
New Idria diapir USA	Disputed (diapiric or sedimentary)	>1 km	x			x	x	x	~1 cm to tens of m	Some	Tsujimori et al. (2007) Wakabayashi (2015)
Mariana forearc mud volcanoes	Diapir	Up to 2 km		x	x				~1 mm to?	No	Maekawa et al. (1995) Pabst et al. (2012)
Northern serpentinite Cuba	Assumed tectonic	?		x		x	x	x	1–10 m	Yes	Garcia-Casco et al. (2006)
Rio San Juan Dominican Republic	Assumed tectonic	?				x	x		0.25 m to 20 m	Yes	Draper et al. (1991) Krebs et al. (2011)
North Motagua Mélange Guatemala	Assumed tectonic	<500 m				x	x	x	~1 m to 100 m	Yes	Flores et al. (2013) Martin et al. (2016) Martens et al. (2017)
South Motagua Mélange Guatemala	Assumed tectonic	<100 m				x	x		<10 m	Some	Tsujimori et al. (2006a) Flores et al. (2013)
Siuna Serpentinite Mélange Nicaragua	Assumed tectonic	Usually <50 m, max 500 m		x		x	x	x	<5 m	Yes	Flores et al. (2015)
Sulawesi Serpentinite Mélange	Assumed tectonic	<500 m			x			x	10 cm–5 m	Yes	Parkinson (1996)
Monviso shear zones Italy	Tectonic	Tens of meters					x		1–10 m blocks ~100 m slivers	Yes	Angiboust et al. (2011)
Cascine Parasi Mélange Voltri Massif, Italy	Tectonic	<100 m				x	x		~5–10 m	Yes	Federico et al. (2007)

et al., 2010; Wakabayashi, 2015), requiring detailed mapping and assessment of the diversity of metamorphic grades, lithologies and matrix to distinguish between them. Among the various kinds of mélange-like units (Table 1), those of Sistan (Eastern Iran) appear unique in that they are probably the best exposed with different metamorphic grades (Angiboust et al., 2013; Fotoohi Rad et al., 2005) and that strikingly clustered Rb/Sr, Ar/Ar and U/Pb ages around 90–85 Ma were found for them ~150 km along the suture (Bröcker et al., 2013).

In order to understand how these sparse and relatively small (~hm scale) blocks of eclogites and HP amphibolites were returned 150 km along strike from seemingly varied depths yet almost coevally, and by which mechanism they formed, we gathered structural, petrological and geochronological data on the Northern exposures of the Sistan metamorphic suture around Gazik. Combining them with former data (Angiboust et al., 2013; Bröcker et al., 2013; Fotoohi Rad et al., 2005; Kurzawa et al., 2017), we then discuss implications for deep-seated mechanisms (e.g., exhumation and/or detachment from the slab; Monié and Agard, 2009) and Sistan geodynamics.

2. Geological setting

2.1. Paleogeographic context

Iran forms a complex network of orogenic belts, testifying to long-lasting convergence (e.g., Stampfli and Borel, 2002; Stöcklin, 1968). The Northern ranges of Iran (Alborz, Kopeh Dagh) formed as a result of Paleozoic to Early Mesozoic convergence of several continental blocks towards Eurasia (e.g., the Cimmerian or Central Iranian Blocks). Southern Iran, on the other hand, was dominated by subduction of the Neotethyan oceanic domain below Eurasia since the Late Jurassic. Although only few remnants are now observed in the Zagros orogen (e.g., Agard et al., 2006; Angiboust et al., 2016), subduction is still ongoing below Makran (Farhoudi and Karig, 1977; Mohammadi et al., 2016b; Saccani et al., 2017). The Sistan orogen, by contrast, results from the closure of a small ocean (i.e., not wider than 1000 km, Barrier et al. (2008); Fig. 1c), probably a former back-arc domain from the Neotethys (Agard et al., 2011) separating the Eurasian platform (i.e., the Afghan Block) from the Cimmerian Lut Block (Fig. 1). Abundant exposures of ophiolite and ocean-related rocks indeed testify to the existence of an early Cretaceous ocean, dated from the early Aptian (~120–115 Ma) to Albian (~110–100 Ma), based on radiolarian fauna (Babazadeh and de Wever, 2004), and early Albian (113–107 Ma) based on zircon U–Pb dating in leucogabbro intrusions in the ophiolite (Zarrinkoub et al., 2012).

The geochemical signature of this ocean is mainly MORB-type (Saccani et al., 2010; Zarrinkoub et al., 2012), although some depleted peridotite samples from the south of the range are interpreted to be the source of supra-subduction zone boninitic melts and may attest to the existence of intra-oceanic subduction from the Turonian to the Maastrichtian (Saccani et al., 2010). This ocean closed in the early Tertiary (Mohammadi et al., 2016a), coeval with the counter-clockwise rotation of the Lut Block (e.g., Mattei et al., 2015). Many structural and magmatic arguments support eastward subduction of the Sistan ocean under the Afghan block (Babazadeh, 2013; Camp and Griffis, 1982; Tirrul et al., 1983) but some studies, based on the wide occurrence and geochemistry of Tertiary magmatic rocks in the Lut block, have argued for westward-dipping (Beydokhti et al., 2015; Pang et al., 2013) or even double-vergent subduction (Arjmandzadeh et al., 2011).

Remnants of this ocean are now part of the Sistan Suture Zone, described by Tirrul et al. (1983) as a Cretaceous to Oligocene subduction-derived accretionary complex. This zone is divided in three geological units: the Ratuk complex (in the East) and the Neh complex (in the West) are both partly overlain by the Sefidabeh basin, regarded as a former forearc basin. The Ratuk and Neh complexes expose oceanic rocks, ophiolite-like units of basalt and peridotite in the Neh complex, and block-in-matrix complexes in the Ratuk complex. Both sides of the orogen termination display en-échelon structures formed as a result of long-lived right-lateral movements from at least the Oligocene to present (Fig. 1; Berberian et al., 2000; Freund, 1970; Jentzer et al., 2017; Sadeghian et al., 2005; Tirrul et al., 1983).

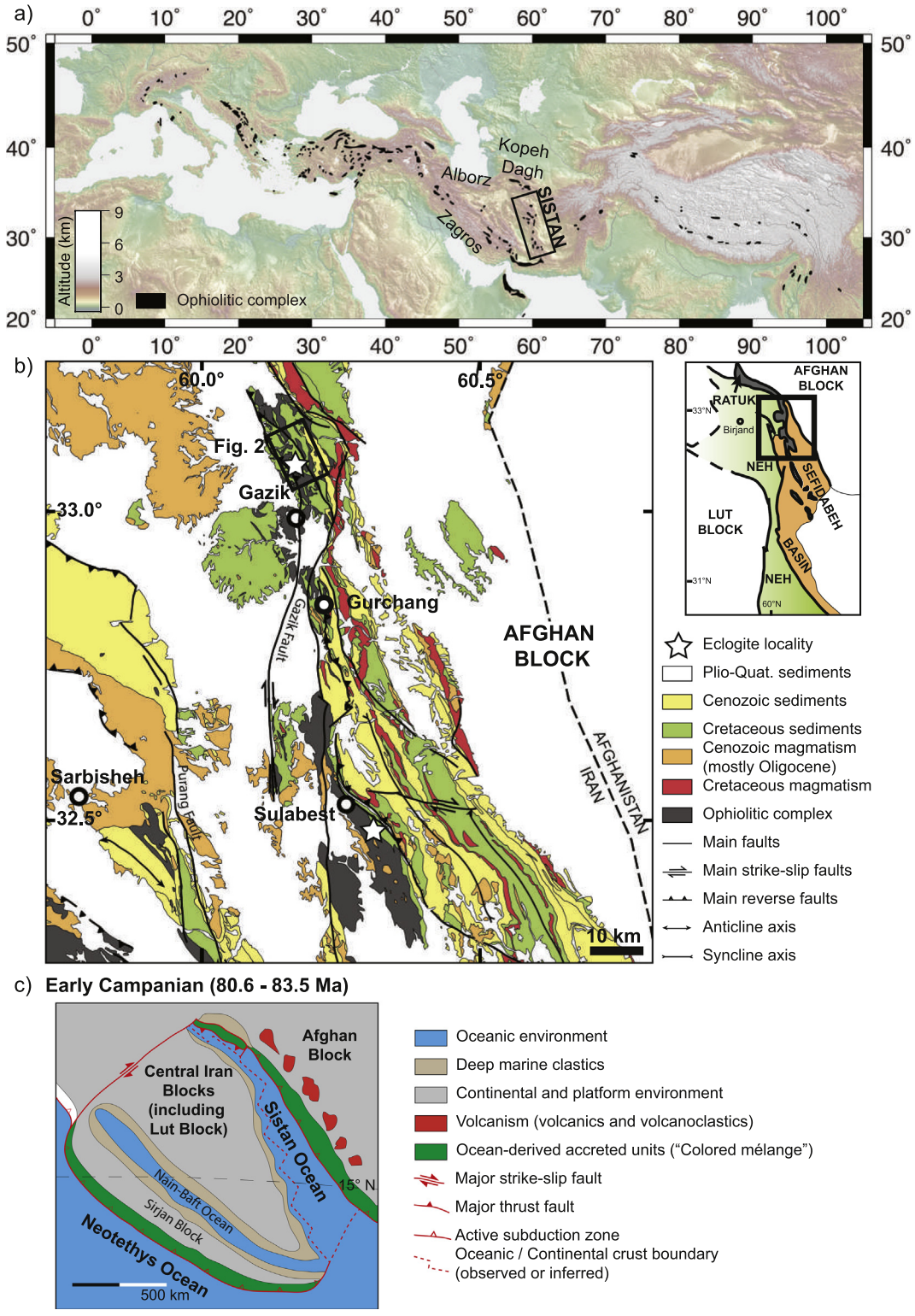

Fig. 1. a) Map of ophiolitic complex in Eurasia, underlining the continuity of ophiolite outcrops along thousands of kilometers, as remnants of different segments of the Neotethys Ocean. The Sistan ophiolitic complex appears as a North-South-trending branch of the Neotethys, orthogonal to the Zagros to the Southwest, and to the Makran ophiolites to the Southeast; b) Sistan geological map centered on the Ratuk complex and block-in-matrix complexes of Gazik and Sulabest (modified from Jentzer et al., 2017); c) Early Campanian paleogeography of Iran (modified from Barrier et al. (2008) showing the Sistan as a branch of the Neotethys Ocean subducting under the Afghan block.

2.2. The Ratuk complex

At the eastern edge of Sistan, the suture zone is marked by the Ratuk complex (Fig. 1b) and bound to the East by the Afghan block (represented by Aptian-Albian Orbitolina limestone, Upper Cretaceous andesitic to basaltic lavas and rare basement rocks; Tirrul et al., 1983), and overlain in places by sediments of the Sefidabeh basin. Three main outcrops of oceanic-derived units are described for the Ratuk complex in the literature, from North to South: Gazik (around N33°03′, E60°15′), Gurchang (N32°53′, E60°15′), and Sulabest (N32°30′,

E60°20′). The main sedimentary rock type outcropping in the suture units of the Ratuk complex is an Upper Cretaceous flysch made of siliciclastic rocks (Nâini et al., 1981) locally containing blocks of a dismembered ophiolite (mainly basalt and radiolarite).

Serpentinite hosting variable amounts of metamorphic blocks crops out in several places (Upper and Eclogitic Units from Angiboust et al., 2013). Pressure-Temperature (P-T) conditions for the enclosed blueschist to eclogite facies exotic blocks were first estimated by Fotoohi Rad et al. (2005) using Average P-T calculations. In Sulabest, they record a peak around 400–650 °C, 1.7–2.7 GPa for the eclogites. Based on pseudosection modelling and Average P-T estimates, (Angiboust et al., 2013) constrained P-T conditions in Sulabest at ca. 500–650 °C, 2.2–2.6 GPa for peak burial, and around 500–650 °C, 0.6–1.3 GPa for the epidote-amphibolite overprint. More recently, zirconium-in-rutile and titanium-in-zircon data for Sulabest eclogites yielded scattered temperatures around 500–600 °C (Kurzawa et al., 2017).

Less attention has been paid to lower grade rocks, especially the amphibolitized blueschists of Sulabest. Fotoohi Rad et al. (2005) estimate the equilibration of one rock at 500–550 °C, 0.6–0.8 GPa, and Angiboust et al. (2013) got P-T conditions of retrogression from blueschist facies for similar rocks of Sulabest at 460–490 °C, ~0.8 GPa using Raman Spectroscopy on Carbonaceous Material (RSCM, Beyssac et al., 2002) and pseudosection modelling.

Peak P-T conditions for the eclogites in Gazik are much less well-constrained (around 400–630 °C, 1.6–2.4 GPa; Fotoohi Rad et al., 2005), and no estimate is provided for the amphibolitized blueschists.

Early Cretaceous exhumation ages were first assumed for this unit using the Ar–Ar method on mica and amphibole (Fotoohi Rad et al., 2009). More recent studies attributed these ages to analytical errors and reappraised eclogite and amphibolitized blueschist ages at around 87–85 Ma using a combination of mica-matrix minerals Rb–Sr isochrons, Ar–Ar, and U–Pb on zircon (Bröcker et al., 2013; Kurzawa et al., 2017). A second retrogression stage involving secondary biotite crystallization in eclogite and amphibolitized blueschist occurs around 83–78 Ma and may last until 75 Ma (Bröcker et al., 2013; Kurzawa et al., 2017).

3. Structural context: mapping and cross-section

Despite attempts to map out the block-in-matrix complexes using remote sensing (via satellite hyperspectral data; e.g., Moeinzadeh, 2015), systematic field investigation and mapping is required to provide a spatially and compositionally accurate map at the m- to hm-scale and distinguish original mélange structures from quaternary slope instabilities (Oligo-Miocene quartz-diorite plutons intruding the metamorphic units also add to the complexity of the area). This study reports on blocks and matrix from two main zones, ~10 km along the suture zone near Gazik (Fig. 2a; with high block density and minimal landsliding). Fig. 2b features the petrological variety of the blocks and the nature of the matrix, which allows recognizing three distinct units: an unmetamorphosed Cretaceous flysch, a slightly metamorphosed siliciclastic-matrix complex (equivalent to the Western Unit of Sulabest), and a serpentinite-matrix complex (equivalent to the Upper and Eclogitic Units of Sulabest; Angiboust et al., 2013). For both complexes blocks are structurally embedded in the matrix. Block-in-matrix relationship needs to be distinguished from common Quaternary landsliding due to relatively steep current slopes in the suture area. These areas are marked by rougher topography and concentration of broken blocks in talwegs. These blocks can locally be embedded in a different matrix than their primary matrix. The synthetic cross-section of Fig. 2c and the outcrop of Fig. 3a show, from top to bottom:

- unmetamorphosed Maastrichtian flysch-type sediments, which were deposited unconformably on all underlying units (siliciclastic-matrix and serpentinite-matrix complexes), as shown by the meter-thick layer of basal conglomerate made of ~10 cm peridotite (Fig. 3b and c) and ophiolitic clasts (Maurizot, 1980).
- the upper block-in-matrix complex, with a very deformed Upper-Cretaceous siliclastic matrix (Maurizot, 1980) mostly made of fine-grained metasandstones with more tuffaceous, albite-rich horizons in places. The matrix hosts slightly metamorphosed blocks of various lithologies (serpentinized peridotite, basalt, sandstone, radiolarite, marls, Fig. 3d), mostly 1–10 m in diameter. This forms a 100–1000 m thick unit overlying the serpentinite-matrix unit, with many tectonic windows, although the nature of the contact between the two units is unclear. This unit could be an equivalent of the Western Unit of Sulabest (Angiboust et al., 2013).
- the lower block-in-matrix complex, with serpentinite as a matrix (with some more tuffaceous parts in places). This unit is a few hundred meters thick. Some serpentinite bodies exhibit deformation gradients. Blocks comprise massive mafic bodies (Fig. 3e) with flattened pillow structures visible on some freshly cut surfaces; Fig. 3f), strongly lineated metatuffaceous mafic rocks and metacherts. They are metamorphosed in blueschist then epidote-amphibolite facies (Fig. 3g) or eclogite facies. Eclogites are structurally below the amphibolitized blueschist. Block size is usually between 1 and 10 m, but can be up 50 m for amphibolitized blueschist-facies blocks, and reaches 150–250 m for two large coherent eclogite bodies. The largest blocks have a North-South elongation, as well as some smaller metatuffaceous blocks. Amphibole-biotite-rich rinds round eclogite blocks. Lineations of the deformed blocks are not coherent (Fig. 2b). This unit corresponds to a combination of the Upper Unit (metatuffaceous rocks) and Eclogitic Unit of Sulabest (Angiboust et al., 2013).

4. Petrography and mineral chemistry

This study focuses only on the metamorphic rocks observed in the block-in-matrix complexes. In the deformed siliclastic-matrix complex, blocks of sandstone, radiolarite and basalt show low grade metamorphism, at maximum greenschist-facies. In the serpentinite, all rocks are metamorphic but evidence a great diversity both in grade (mafic eclogites, amphibolitized blueschist) and lithology (basalt, tuff, chert). We describe below the petrography, mineralogy and chemistry of these metamorphic rocks. Mineralogical occurrences and coordinates of samples are given on Table 2 and all mineral abbreviations are in Supplementary data S1.

4.1. Petrography

In the siliciclastic-matrix, metamorphism is mostly visible in mica-rich portions of the matrix and in greenschist basalt. The matrix is mainly composed of quartz, albite, chlorite, organic matter and rare phengite (for ex, 15b05, Fig. 4a). It is highly folded and crenulated.

Greenschist-facies metabasalts are found as large blocks (>10 m) in the siliciclastic-matrix complex. They are fine-grained and recrystallized with chlorite, biotite, actinolite, albite and epidote.

In the serpentinite matrix, we distinguish four kinds of metamorphic rocks, defined by their protolith and metamorphic grade: (1) eclogitic metabasalt, (2) amphibolitized blueschist, (3) blue amphibole-bearing metachert, (4) Ca–Na pyroxene-albite rocks. The serpentinite itself contains in some places some long (~10 cm) fibers of antigorite, as well as some talc or chlorite-actinolite-rich portions (Fig. 3h).

(1) Eclogite-facies metabasalts are found as large two blocks in the Western part of the serpentinite-matrix complex in Gazik. Samples show various retrogression stages. The freshest eclogite

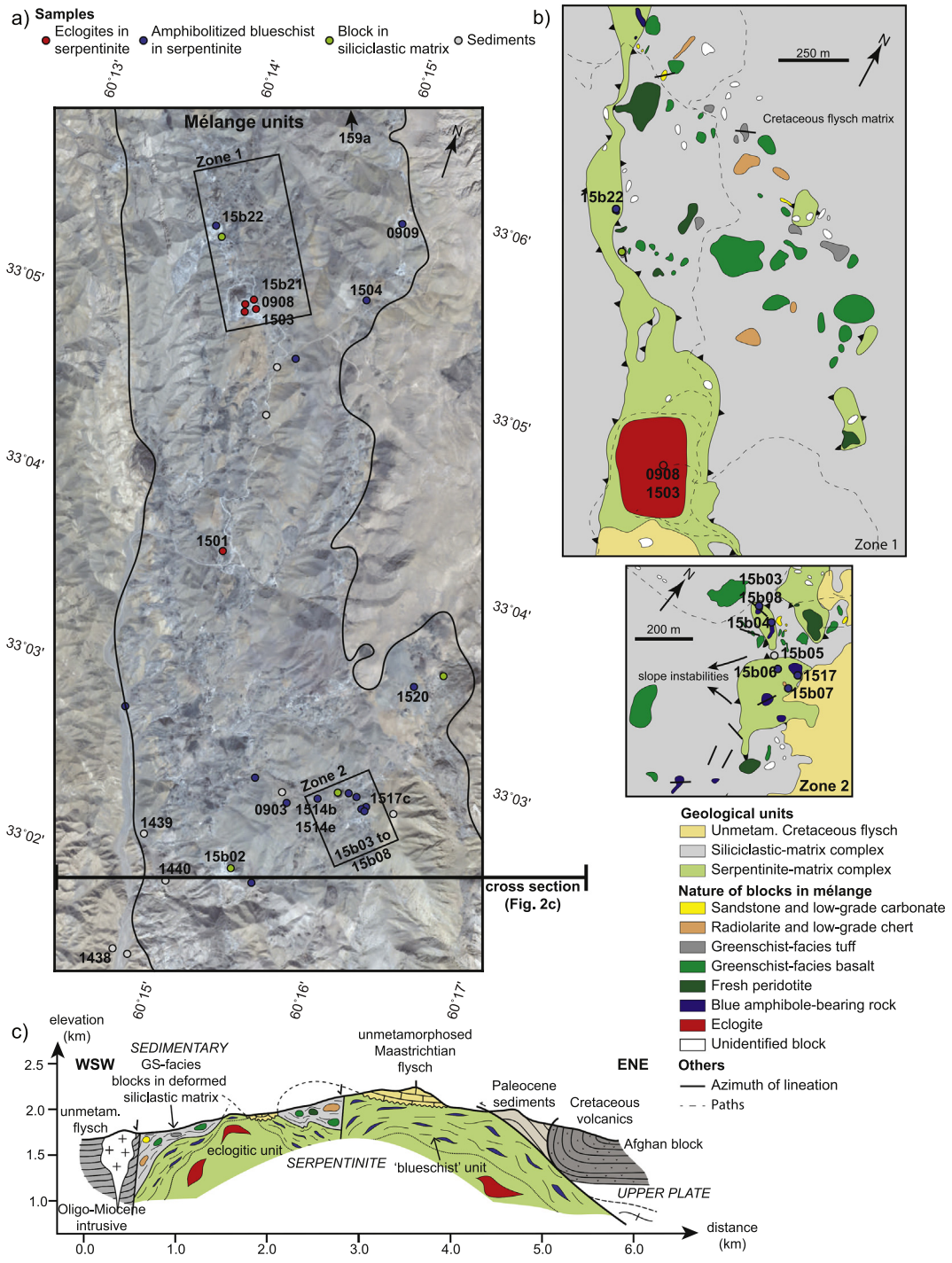

Fig. 2. a) Localization of samples in the Gazik area of the block-in-matrix complexes; b) Detailed mapping of two zones in Gazik; (c) Synthetic cross-section of the suture units in Gazik.

(sample 0908, Fig. 4b) is made of garnet in a matrix of omphacite. Small inclusions in garnet are omphacite, phengite and clinozoisite. Rutile in the matrix is partly retrogressed to titanite. Some samples show more extensive retrogression with albite rims around garnet, and blue-green amphibole (like barroisite or winchite) replacing omphacite in the matrix (e.g., 1503, Fig. 4c). In one sample (1501), retrogression is marked by darker ferric pyroxene in the matrix and atoll-shaped garnets. Glaucophane inclusions in garnet and hornblende were found in some samples (Fig. 4d). Fresh lawsonite is found in garnet cores of one sample (Fig. 4e), associated with omphacite (Fig. 4f). Most samples only have lawsonite pseudomorphs, occurring as subhedral, lozenge-shaped inclusions of Fe^{3+}-poor clinozoisite and paragonite in garnet (Fig. 4g; Angiboust and Agard, 2010; Tsujimori et al., 2006b). These pseudomorphs are found in all parts of garnets, but not in the matrix.

(2) Amphibolitized blueschist is the dominant block type in the serpentinite-matrix complex. These blocks are variably deformed, from almost static (1514b, Fig. 5a) to very schistosed (1514e, Fig. 5b). The protoliths of these rocks can be recognized in places as hydrothermalized pillow basalt or mafic volcano-sedimentary rocks ("tuffs"). They are made of blue-green amphibole with

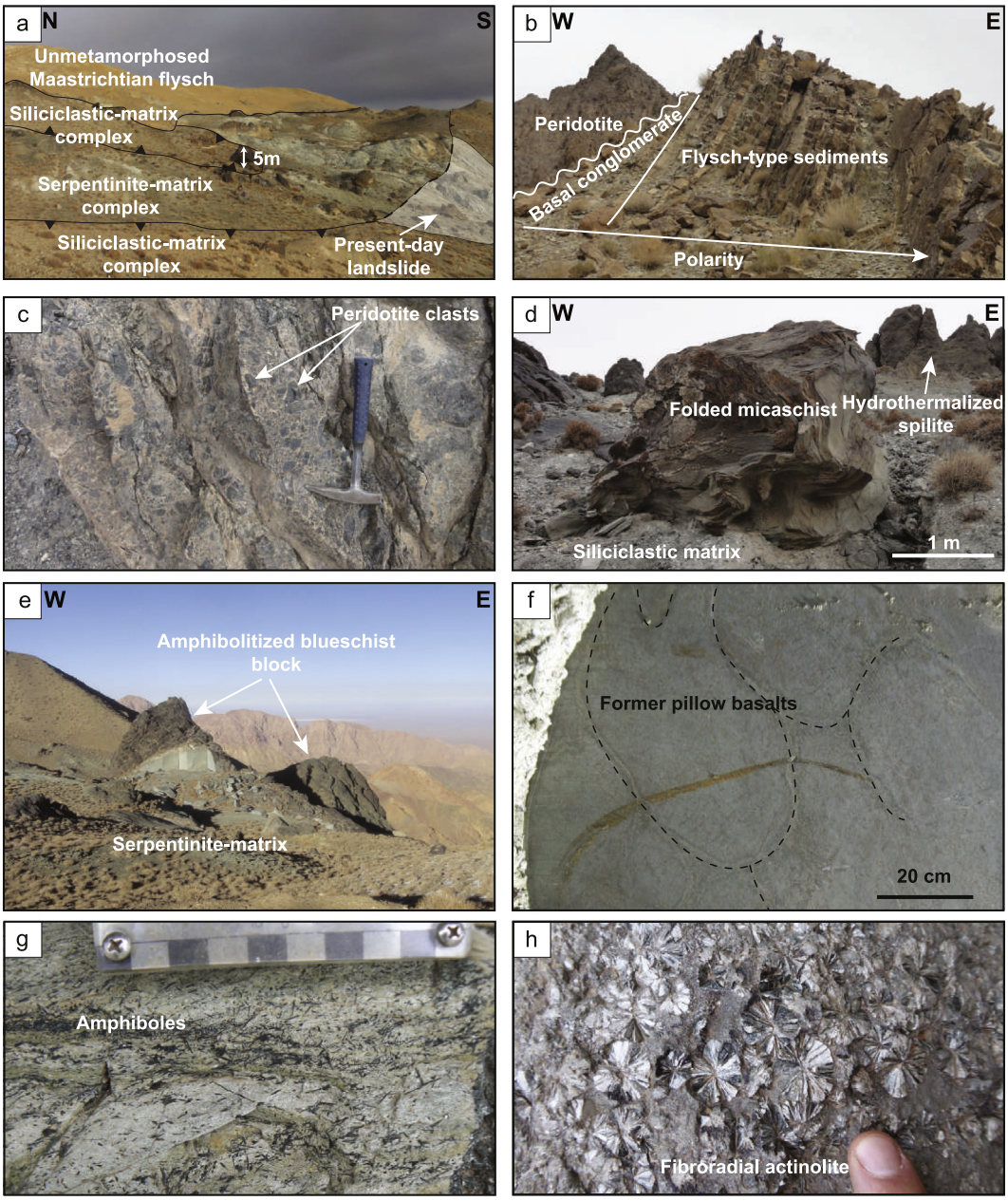

Fig. 3. Pictures of outcrops in Gazik: a) Global structure of the block-in-matrix complexes; b) Sedimentary contact between Maastrichtian flysch-type sediments and serpentinized peridotite from a ~300 × 150 m, less dismembered part of the serpentinite-matrix complex; c) Peridotite clasts at the contact between Paleocene and peridotite of Fig. b; d) Folded greenschist-facies micaschist and basaltic block in siliciclastic mélange, e) Block of amphibolitized blueschist in serpentinite; f) Preserved pillow structures in amphibolitized blueschist; g) Amphibolitized blueschist of the serpentinite-matrix complex composed of albite matrix, large calcium-sodium amphibole crystals, phengite and epidote crystals. The scale is 5 cm-long; h) Fibroradial actinolite associated with chlorite in the serpentinite.

rare green then blue amphibole (Fig. 5c) cores. Blue-green amphibole and phengite often make a strong foliation in an albite-rich matrix. Epidote is commonly abundant. One sample has small crystals of clinopyroxene replacing amphibole (0909, Fig. 5d). Garnet is found in some of these rocks but contains no inclusions and is partially retrogressed in stilpnomelane (1504, Fig. 5e). Biotite can occur as a retrograde phase in some samples (15b22). The main titanium-bearing mineral is titanite. The intensity of deformation correlates with the amount of mica.

(3) Blue amphibole-bearing metachert (Si1517c, Fig. 5f) is a quartz-rich rock, in which two generations of blue amphibole with different orientations associated with phengite make a strong foliation. The rock contains small garnets and highly retrogressed clinopyroxene and alkaline feldspar. The retrogression transformed amphibole and mica into chlorite.

(4) One block of aegirine-augite-albite rock was found (15b03, Supplementary material S2). Small crystals of blue amphibole and phengite are also found in the matrix. In this rock, deformation is localized along a shear zone with recrystallized albite.

4.2. Mineral chemistry

Analyses were carried out on the electron microprobes Cameca SX-5 and SX-100 at iSTeP and JEOL-JXA 8230 at GFZ Potsdam. All analyses were sorted, and structural formulae calculated with Fe^{3+} estimates

Table 2
Coordinates and minerals in analyzed and/or dated minerals.

Sample	Locality	Gt	Cpx	Ca-Amp	Ca-Na-Amp	Na-Amp	Ph	Bt	Ep	Ab	Chl	Qz	Rt	Ttn	Accessory	Latitude	Longitude
0903	Gazik			x	x		x			x	x			x	Cal	33.0433°	60.2589°
0908	Gazik	x	x	x	x	x	x		x	x	x		x	x	Cal	33.0864°	60.2394°
0909	Gazik		x	x	x		x		x	x	x			x	Cal	33.098°	60.2522°
1438	Gazik											x			Cal, Organic Matter	33.0256°	60.2452°
1439	Gazik						x				x	x			Cal, Organic Matter	33.0367°	60.2448°
1440	Gazik						x				x	x			Organic Matter	33.0331°	60.2486°
1501	Gazik	x	x	x			x	x	x	x			x	x	Op	33.064°	60.2439°
1503	Gazik	x	x	x	x	x	x		x	x	x		x		Pg, Op	33.0865°	60.2381°
1504	Gazik	x				x				x					Stp, Op	33.0902°	60.2509°
1509a	Gazik					x	x		x	x	x		x	x	Op	33.119°	60.2439°
1514b	Gazik				x		x	x	x	x	x			x	Op	33.0446°	60.262°
1514e	Gazik			x	x		x		x	x	x			x	Or	33.0446°	60.262°
1517c	Gazik	x	x			x	x					x		x	Or	33.0452°	60.2674°
1520	Gazik					x	x		x	x	x				Cal, Ox	33.0568°	60.2696°
15b02	Gazik			x				x	x	x	x					33.0353°	60.2546°
15b03	Gazik		x		x		x			x						33.0459°	60.2652°
15b04	Gazik				x	x	x		x	x	x		x	x	Ilm, Op	33.0458°	60.2661°
15b05	Gazik						x			x	x	x			Cal	33.0453°	60.2664°
15b06	Gazik				x		x			x	x				Cal	33.0449°	60.267°
15b07	Gazik				x					x	x				Cal, Ox	33.0447°	60.2674°
15b21a	Gazik	x		x	x	x			x	x				x	Ox	33.0872°	60.2389°
15b21c	Gazik	x		x	x				x	x	x				Ox	33.0872°	60.2389°
15b21d	Gazik	x	x	x	x	x	x		x	x	x		x	x	Lws, Pg, Ox	33.0872°	60.2389°
15b22	Gazik			x	x			x		x	x			x	Cal, Op	33.0927°	60.2325°
15bα	Sulabest	x			x										no thin section	32.5109°	60.3452°
Su-n	Sulabest	x	x	x	x		x		x	x	x		x	x	Ox	32.5087°	60.3493°
Su0902	Sulabest	x	x	x	x		x		x	x			x		Ox	32.5083°	60.3464°
Su0906	Sulabest			x	x		x	x		x	x		x			32.5046°	60.3529°
Su0909	Sulabest				x		x			x	x				Ox	32.5114°	60.3486°
Su0910	Sulabest				x		x		x	x	x					32.5114°	60.3486°
Sum8	Sulabest				x		x	x	x	x	x				Ox	32.5128°	60°3457°

using the method of Droop (1987) for garnet and clinopyroxene, and the method exposed in Leake et al. (1997) for amphibole. We considered all iron as ferric in epidote and lawsonite, and as ferrous in mica. All analyses are plotted in Fig. 6 and representative analyses are shown on Table 3.

4.2.1. Garnet

Garnet (Fig. 6a) is found in eclogites, amphibolitized blueschist and blue amphibole-bearing metachert. In eclogite, garnet is almandine-rich, with strong zoning from a spessartine-rich-pyrope-poor core (up to 18% spessartine) to a rim richer in pyrope (up to 16 mol% pyrope). Some samples show the full zoning (1503) whereas others show only parts of it (1501 for the early part, 0908 for the pyrope-richer part). In the amphibolitized blueschist sample, garnet is manganese-rich almandine (about 22 mol% spessartine), slightly richer in manganese in the core than in the rim (for example sample 1504, Fig. 5d). In amphibole-bearing metachert, garnet is hydro-spessartine (around 2.5 wt% water, 54 mol% spessartine).

4.2.2. Clinopyroxene

Clinopyroxene (Fig. 6b) is found in eclogite as omphacite (for example 0908, 1503) for prograde and peak eclogitic assemblage and as aegirine-augite in retrograde matrix (for example 1501, Fig. 4g). Aegirine-augite is also found in minor quantity in an amphibolitized blueschist (0909, Fig. 5d) and is a major component of the aegirine-augite-albite rock (for example 15b03, Supplementary Material S2). In amphibole-bearing metacherts, clinopyroxene is aegirine.

4.2.3. Amphibole

Amphibole (Fig. 6c) in eclogite forms during different stages of the evolution of the rock. Most of them are late magnesio-hornblende in the matrix, with ~0.50 XFe^{3+} but some have a blue core of Fe^{3+}-poor glaucophane (XFe^{3+} ~0.20). In amphibolitized blueschist, amphiboles are usually more ferric (minimum $XFe^{3+} = 0.30$, and up to 1.00). These amphiboles have a very wide range of ^{B}Na content (from 0.1 to 1.7 atoms per formula unit - apfu) but mostly plot in the barroisite field. Preserved actinolite cores in blue amphibole are found in two samples (15b-07 and 15b-08), while glaucophane cores were found in one sample (15b07) of this rock type. Rare amphibole in the pyroxene-albite rocks is ferri-winchite. In amphibole-bearing metachert, dark blue to purple amphibole is magnesioriebeckite (XFe^{3+} ~0.70). Amphibole in greenschist-facies metabasalt of the siliciclastic-matrix complex is ferri-actinolite ($XFe^{3+} > 0.70$).

4.2.4. Mica

White mica is found in almost every sample, except greenschist-facies metabasalts. It is always phengitic, i.e. enriched in Si compared to pure muscovite and substituted towards the celadonite end-member (Fig. 6d). In eclogite the maximum ^{T}Si is between 3.5 and 3.6 apfu, but most phengites have ^{T}Si between 3.2 and 3.5. In amphibolitized blueschist, pyroxene-albite rock and amphibole-bearing metachert, ^{T}Si is usually around 3.2 and 3.4 apfu, but can be higher in clinopyroxene-bearing amphibolitized blueschist.

Biotite is an accessory phase of some samples, notably eclogite where it is found as a phase destabilizing garnet (e.g., 15b21d, 1501, 1503) and in greenschist facies metabasalts (for example 15b02) of the siliciclastic-matrix complex. XMg is usually around 0.43 and 0.50 in these rocks.

4.2.5. Epidote

In eclogite and amphibolitized blueschist, epidote shows large variations of compositions between the ferric end-member epidote and clinozoisite (Fig. 6e). In eclogite, the most aluminous epidote is found as inclusions in garnet ($XCzo = (Al - 2) / (Al - 2 + Fe^{3+} + Mn^{3+}) = 85\%$, in a lawsonite pseudomorph), where epidote in the matrix, although zoned, lies between XCzo = 0.45 and

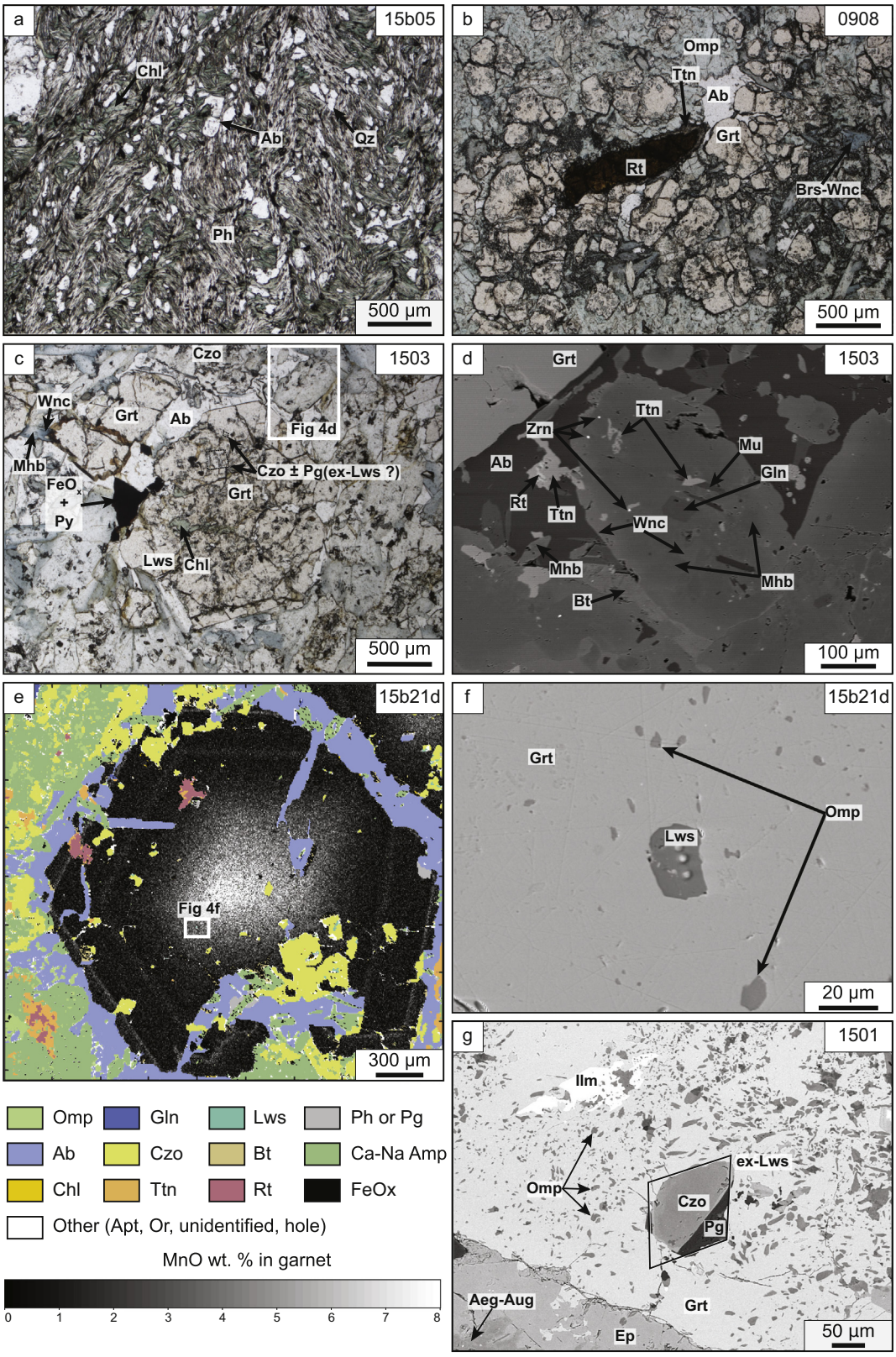

Fig. 4. Photomicrographs and other pictures of samples (1/2). a) Greenschist-facies sandstone; b) Fresh eclogite showing the peak assemblage of Grt-Omp-Rt, and retrogression in Ttn and Ca-Na Amp; c) Euhedral garnet with zoned inclusion pattern, and extensively retrogressed matrix; d) SEM image of a zoned amphibole of eclogite matrix with a Gln core; e) X-ray map interpretation of the mineral assemblage superimposed with Mn zonation pattern in garnet; f) SEM image of lawsonite inclusion in garnet associated with omphacite; g) SEM image of lozenge-shaped inclusion of Czo and Pg in garnet interpreted as Lws pseudomorph.

XCzo = 0.70, with XCzo decreasing from core to rim. In a very oxidized sample (Si15-01), epidote is very ferric (XCzo <0.45). In amphibolitized blueschist, epidote is ferric (XCzo <0.40) except some preserved aluminium rich cores (XCzo ~0.60). In greenschist-facies metabasalt of the siliciclastic matrix, epidote is always very ferric (XCzo <10%).

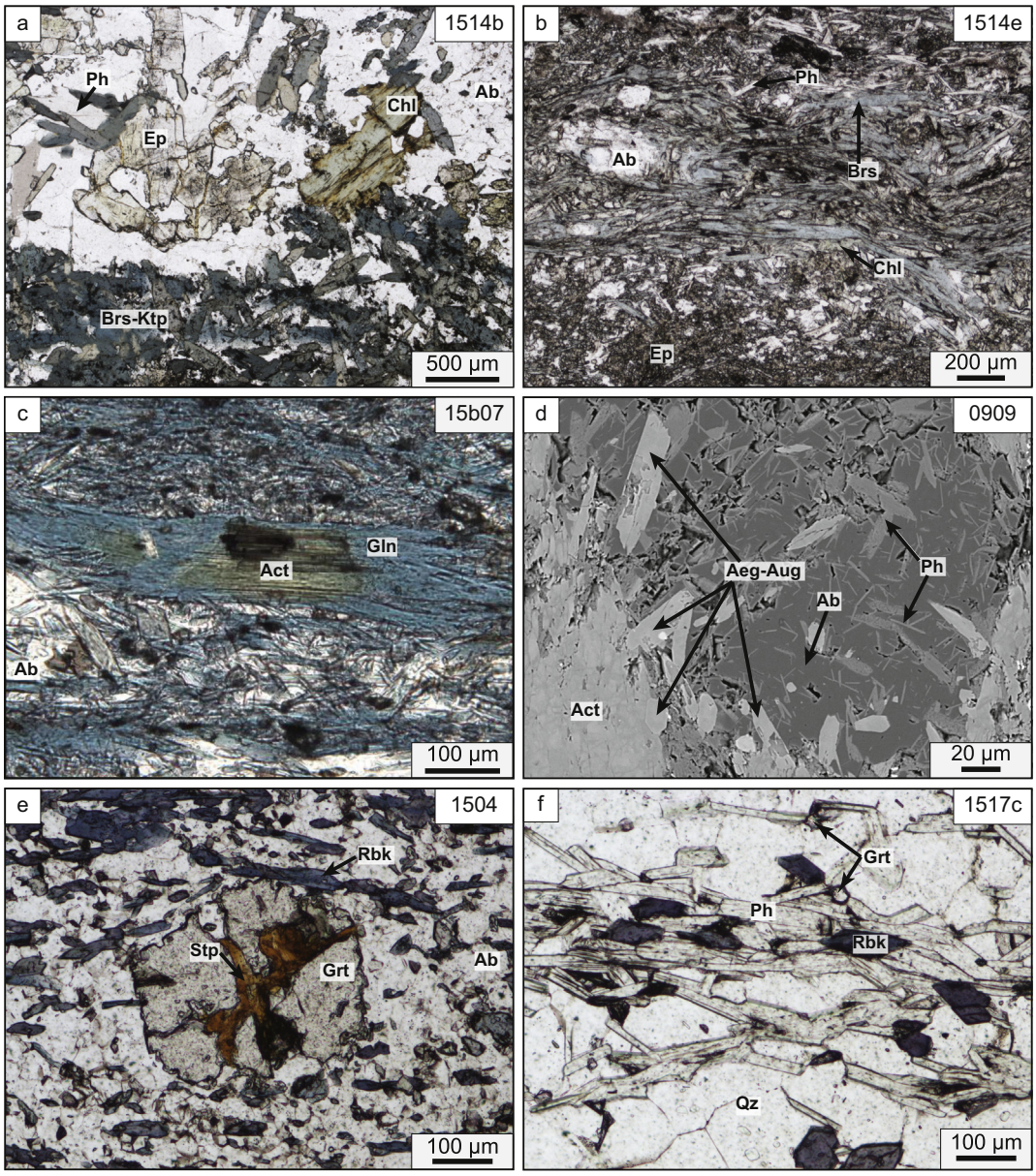

Fig. 5. Photomicrographs and other pictures of samples (2/2). a) Amphibolitized blueschist-facies metabasalt; b) Amphibolitized blueschist-facies metatuff; c) SEM image of clinopyroxene in amphibolitized blueschist-facies metatuff; d) Actinolite cores in glaucophane in amphibolitized blueschist-facies metatuff attesting for a prograde greenschist-facies assemblage; e) Garnet and stilpnomelane in amphibolitized blueschist-facies metatuff; f) Blue amphibole-bearing metachert.

5. Pressure-temperature estimates

5.1. Methods

5.1.1. Tmax estimates by Raman spectroscopy on carbonaceous matter (RSCM)

The RSCM thermometry allows determination of the maximum temperature (Tmax) reached by the carbonaceous matter in a sample in the range 200–650 °C, with an intrinsic error of ±50 °C (Beyssac et al., 2002; Lahfid et al., 2010). This method is used to determine the maximum temperature reached by the siliciclastic-matrix complex. In most samples, carbonaceous matter is oxidized, which prevents temperature estimates, but three samples in the suture zone yielded coherent temperatures.

5.1.2. Pressure-temperature estimates

P-T conditions of the eclogite peak and retrograde stage were estimated using two different methods: direct thermodynamic modeling (pseudosection calculation), and conventional multiequilibrium thermobarometry.

5.1.3. Average P-T THERMOCALC

Multi-equilibrium thermobarometry was performed using THERMOCALC program in the Average P-T mode (Powell and Holland, 1994). Mineral activities were calculated with the AX software (https://www.esc.cam.ac.uk/research/research-groups/research-projects/tim-hollands-software-pages/ax).

5.1.4. Perple_X thermodynamic modelling

Pseudosections were calculated using Perple_X (6.7.2 version, Connolly, 1990, 2005) using the internally consistent thermodynamic dataset and equation of state of H_2O of Holland and Powell (1998). Solution models considered in the calculation are garnet, epidote, chlorite (Holland et al., 1998), amphibole and clinopyroxene (Diener and Powell, 2012), white mica (Coggon and Holland, 2002), biotite (White

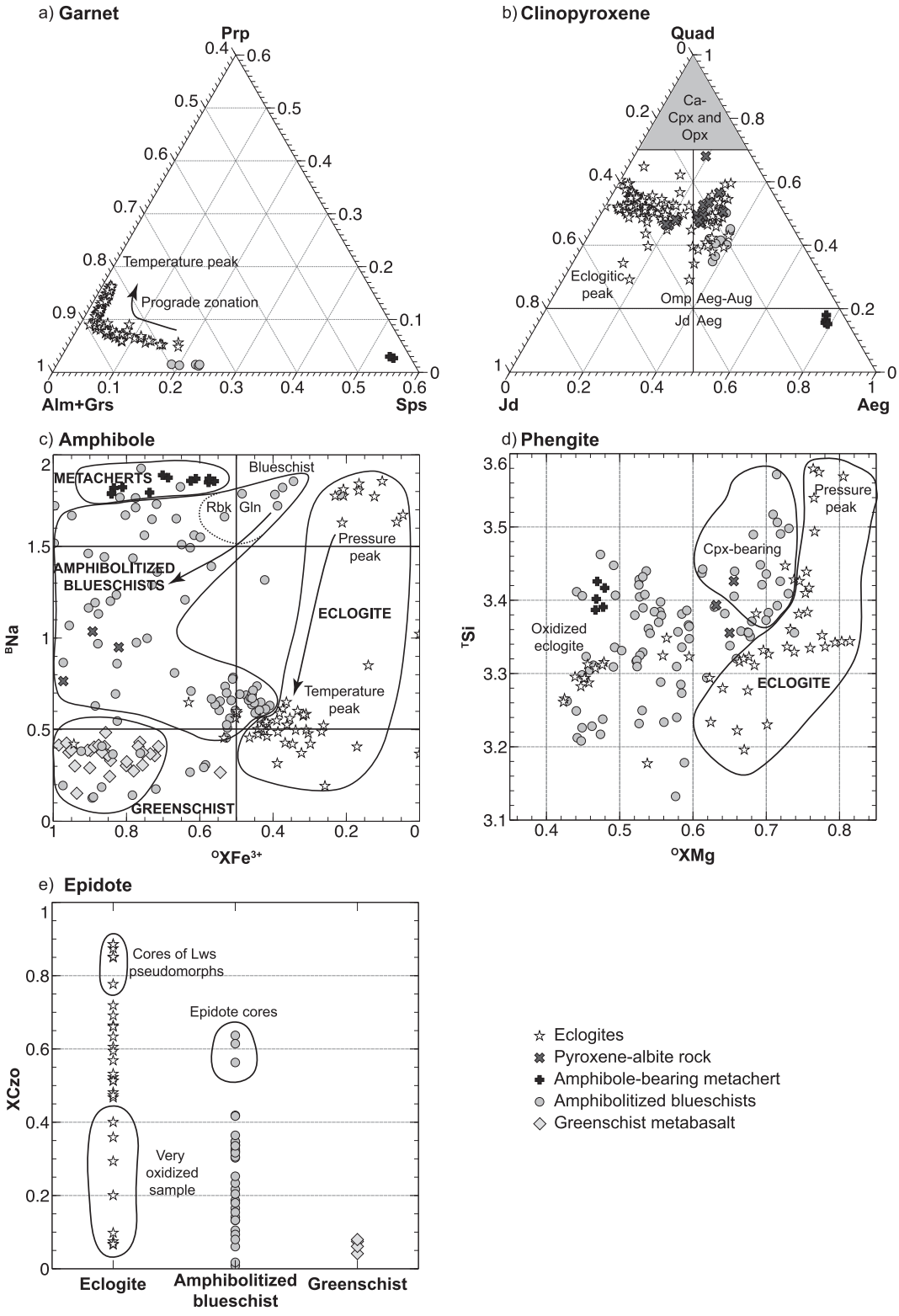

Fig. 6. Compositional plots of minerals: a) Ternary diagram for garnet; b) Ternary diagram for clinoyroxene; c) ^{B}Na versus $^{O}XFe^{3+}$ in amphibole ($^{O}XFe^{3+} = {}^{O}Fe^{3+}/({}^{O}Al + {}^{O}Fe^{3+})$); d) ^{T}Si versus ^{O}XMg diagram of phengite; e) XCzo of epidote in rocks according to their metamorphic grade.

et al., 2007), and talc (Holland and Powell, 1990). The equilibrium composition of our sample is estimated with surface scanning of a fresh part of a thin section with the SEM, and removing the contribution of manganese-rich garnet cores that are not reacting at peak P-T conditions. Trying to simulate this composition thanks to the measured compositions of peak minerals is very satisfactory and gives modal amounts close to the ones observed in thin section. Ferric iron content estimation is very sensitive to the amount of omphacite at peak (considered as the main ferric iron-bearing mineral), but there is also a minor contribution from garnet, lawsonite and phengite. Water content is mainly dominated by the peak modal proportion of lawsonite. Following the method of Groppo and Castelli (2010), we choose to use a best-fit criterion to

Table 3
Representative analyses of the main metamorphic minerals.

Mineral	Gt	Gt	Cpx	Cpx	Amp	Amp	Ph	Ph	Ep	Ep	Lws
Sample	0908	1503	0908	15b03	1503	1514e	1517c	1501	0908	1514b	15b21d
Location	Core	Core	Inclusion in Gt	Matrix	Core	Matrix	Matrix	Matrix	Inclusion in Gt	Matrix	Inclusion in Gt
SiO_2	38.05	36.77	55.35	53.97	57.09	52.24	49.84	48.79	38.06	37.11	38.39
TiO_2	0.00	0.16	0.05	0.00	0.03	0.21	0.51	0.39	0.12	0.13	0.18
Al_2O_3	21.22	20.65	9.01	5.88	10.57	6.35	24.26	27.48	30.61	23.77	31.59
Cr_2O_3	0.00	0.00	0.07	0.00	0.04	0.03	0.03	0.03	0.01	0.00	0.00
FeO	28.49	28.42	7.45	11.59	9.28	11.13	6.19	5.87	4.93	11.97	0.96
MnO	0.87	4.89	0.08	0.52	0.08	0.27	0.13	0.05	0.11	0.28	0.08
MgO	3.42	1.67	8.39	7.81	11.33	14.66	3.20	2.78	0.08	0.00	0.01
CaO	7.95	7.77	13.62	12.79	1.33	8.97	0.04	0.03	23.60	22.96	16.84
Na_2O	0.02	0.08	6.45	6.93	6.83	3.27	0.30	0.43	0.00	0.01	0.03
K_2O	0.00	0.01	0.00	0.00	0.01	0.12	10.52	10.85	0.00	0.00	0.00
Total	100.02	100.42	100.47	99.51	96.61	97.25	95.00	96.70	97.52	96.23	88.15
#(O, OH)	12	12	6	6	23	23	11	11	12.5	12.5	8
Si	3.01	2.96	2.00	2.02	7.87	7.44	3.42	3.29	2.93	2.97	2.02
Ti	0.00	0.01	0.00	0.00	0.00	0.02	0.03	0.02	0.00	0.00	0.00
Al	1.98	1.96	0.38	0.26	1.72	1.07	1.96	2.18	2.78	2.24	1.96
Cr	0.00	0.00	0.00	0.00	0.00	0.00	0.00	0.00	0.00	0.00	0.00
Fe^{3+}	0.02	0.17	0.11	0.31	0.32	0.35	0.00	0.00	0.32	0.80	0.04
Fe^{2+}	1.87	1.74	0.12	0.06	0.75	0.98	0.35	0.33	0.00	0.00	0.00
Mn	0.06	0.33	0.00	0.00	0.01	0.03	0.00	0.00	0.01	0.02	0.00
Mg	0.40	0.20	0.45	0.44	2.33	3.11	0.33	0.28	0.00	0.00	0.00
Ca	0.67	0.67	0.53	0.51	0.20	1.37	0.00	0.00	1.95	1.97	0.95
Na	0.00	0.00	0.45	0.50	1.83	0.90	0.04	0.06	0.00	0.00	0.00
K	0.00	0.00	0.00	0.00	0.00	0.02	0.92	0.93	0.00	0.00	0.00
Comp.	$Grs_{21.5}Prp_{13.5}Alm_{62}Sps_2Adr_1$	$Grs_{17.5}Prp_{6.5}Alm_{60.5}Sps_{11}Adr_{4.5}$	$Jd_{37}Ae_{10}Quad_{53}$	$Jd_{24}Ae_{29}Quad_{47}$	Gln	Brs	$Mus_{64}Cel_{36}$	$Mus_{79}Cel_{21}$	$Czo_{69}Ep_{31}$	$Czo_{20}Ep_{80}$	Lws

adjust the quantities of ferric iron and water. This results in a ferric iron percentage of 20 mol% of the total iron, with 1.6 wt% of water, close to water excess, as suggested by the stability of lawsonite (Clarke et al., 2006). For sample 0908, the following composition was used (in oxide weight percentage): SiO_2 (50.47%), Al_2O_3 (13.90%), FeO (10.00%), Fe_2O_3 (2.775%), MgO (5.11%), CaO (12.10%), Na_2O (3.72%), K_2O (0.27%), H_2O (1.60%).

For various reasons discussed below, no P-T conditions could be obtained for other high-grade rocks.

5.2. Results

5.2.1. Siliciclastic-matrix complex

The RSCM method yielded results for three samples (Table 4). Sample 1438, located in units to the West of the block-in-matrix complexes, shows a maximum temperature of 240 °C. Samples 1439 and 1440 collected in the siliciclastic-matrix complex reached a higher temperature around 340 °C.

Average P-T calculation on greenschist-facies metabasalts (15b02) with an actinolite-biotite-albite-chlorite-epidote – water assemblage yields a temperature of 407 ± 163 °C and a pressure of 0.67 ± 0.16 GPa (cor = 0.687, sigfit = 0.59, cutoff = 1.73). Fotoohi Rad et al. (2005) estimated the P-T conditions at 420 °C and 0.3 GPa.

Table 4
Synthesis of RSCM temperatures. n is the number of good spectra for each sample, σT is the standard deviation of the temperature, $\sigma T/\sqrt{(n-1)}$ is a statistical test to probe the quality of the temperature calculation, it is good if <8, LT refers to the low temperature calibration, HT to the high-temperature one.

Sample	T_{max} (°C)	n	R or R2	σT (°C)	$\sigma T/\sqrt{(n-1)}$	Method
1438	240	13	0.995	14	4.1	LT
1439	339	27	0.680	4.1	0.8	HT
1440	343	11	0.670	7.3	2.6	HT

5.2.2. Eclogite

The peak of eclogites has been determined using Average-P-T calculations, with the assemblage garnet-omphacite-lawsonite-phengite-quartz-water. Inclusions in the mantle of garnet have been used to determine the peak P-T at 526 °C ± 23 °C and 2.27 ± 0.14 GPa (cor = 0.891, sigfit = 0.02, cutoff = 1.73).

The retrograde path is calculated with Thermocalc and the epidote-amphibolite mineral assemblage: hornblende-epidote-muscovite-albite-water. The peak temperature is estimated at 531 ± 62 °C and 0.89 ± 0.2 GPa (corr = 0.939, sigfit = 0.55, cutoff = 1.73).

Fig. 7a shows the pseudosection, with the best-fit area of the isopleths at eclogitic facies, around 526 °C and 2.31 ± 0.03 GPa superimposed with the ellipses of Average P-T calculations. The best fit of the isopleths is in the garnet-omphacite-phengite-lawsonite-talc-quartz ± water field. There is a very good correspondence between the predicted and observed composition and modes of minerals.

These P-T estimates for the peak are similar to those made by Fotoohi Rad et al. (2005) using only Average P-T calculations, but the use of two largely independent methods gives a confidence in the methods used and in the chosen equilibrium assemblages. Fotoohi Rad et al. (2005) do not estimate P-T conditions of the post-peak epidote-amphibolite assemblage.

P-T estimates for the eclogites are superimposed with those from the literature and compared with those of Sulabest in Fig. 7b.

5.2.3. Amphibolitized blueschist

Epidote-amphibolite assemblages are found either in massive metabasalts or in more schistosed mafic rock. No reliable P-T estimate could be obtained on these rocks, mostly because of intense oxidation during retrogression.

The peak mineral assemblage of these rocks is at blueschist facies with relict glaucophane and clinozoisite-rich epidote, and inclusions of actinolite attest of the prograde greenschist-facies assemblage. Most of the samples have been pervasively recrystallized at epidote-amphibolite grade, with a common mineral assemblage involving

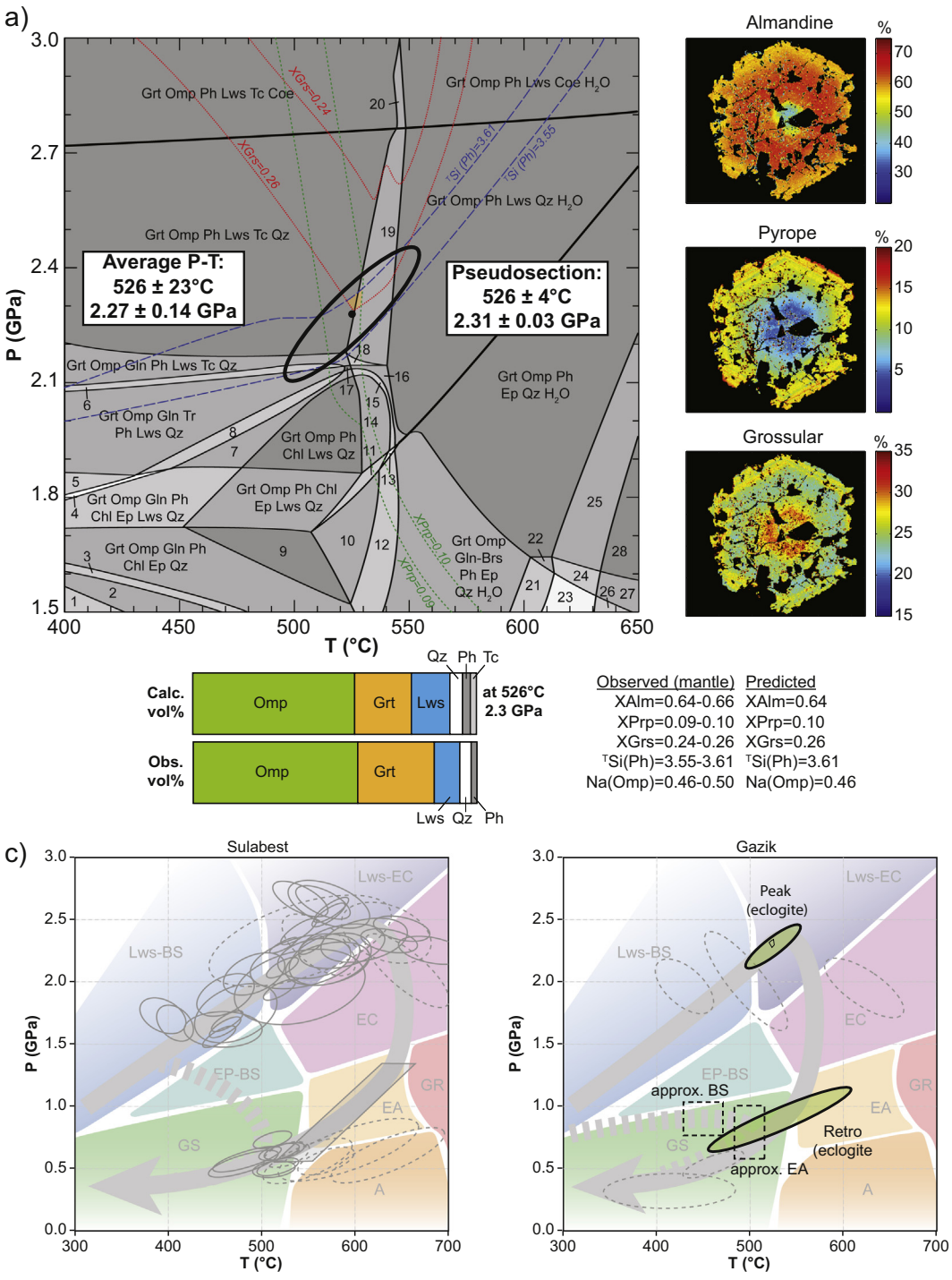

Fig. 7. a) Pseudosection on eclogite 0908 of Gazik. Filling of the fields corresponds to variance, from 2 to 5. Darker fields have higher variance. Blue isopleths are for Si content (apfu) in phengite, red is for grossular content of garnet, green for pyrope content in garnet. The orange zone is the best-fit area of the pseudosection, the ellipse is the result of Average P-T calculation. Legend of the fields: 1: Grt Omp Tr Gln Bt Chl Ep Qz, 2: Grt Omp Gln Bt Chl Ep Qz, 3: Grt Omp Gln Ph Bt Chl Ep Qz, 4: Grt Omp Gln Tr Ph Chl Ep Lws Qz, 5: Grt Omp Gln Tr Ph Ep Lws Qz, 6: Grt Omp Gln Tr Ph Lws Tc Qz, 7: Grt Omp Gln Ph Chl Lws Qz, 8: Grt Omp Gln Tr Ph Chl Lws Qz, 9: Grt Omp Ph Chl Ep Qz, 10: Grt Omp Ph Chl Ep Qz H2O, 11: Grt Omp Ph Chl Ep Lws Qz H2O, 12: Grt Omp Gln Ph Chl Ep Qz H2O, 13: Grt Omp Gln Ph Chl Ep Lws Qz H2O, 14: Grt Omp Ph Chl Lws Qz H2O, 15: Grt Omp Gln Ph Chl Lws Qz H2O, 16: Grt Omp Gln Ph Lws Qz H2O, 17: Grt Omp Gln Ph Lws Qz, 18: Grt Omp Gln Ph Lws Tc Qz H2O, 19: Grt Omp Ph Lws Tc Qz H2O, 20: Grt Omp Ph Lws Tc Coe H2O, 21: Grt Omp Brs Ph Pg Ep Qz H2O, 22: Grt Omp Ph Pg Ep Qz H2O, 23: Grt Omp Brs Ph Pg Ep Zo Qz H2O, 24: Grt Omp Ph Pg Ep Zo Qz H2O, 25: Grt Omp Ph Ep Zo Qz H2O, 26: Grt Omp Brs Ph Pg Zo Qz H2O, 27: Grt Omp Ph Pg Zo Qz H2O, 28: Grt Omp Ph Zo Qz H2O. X-ray maps of a garnet in sample 0908, modal and mineral compositions show a very good correspondence between analyses and models; b) Synthesis of P-T estimates for the eclogites in Gazik and Sulabest from Fotoohi Rad et al. (2005) in dashed gray ellipses and Angiboust et al. (2013) in solid gray ellipses and pseudosection fields, and new P-T estimates (pseudosection and Average P-T ellipses) in Gazik. Dashed boxes indicate approximate P-T evolution of the amphibolitized blueschists in Gazik are estimates from Diener and Powell (2012). (For interpretation of the references to colour in this figure legend, the reader is referred to the web version of this article.)

barroisite-epidote-albite-titanite ± phengite ± sodic pyroxene ± Mn-rich garnet. The absence of Mg-rich garnet at equilibrium with sodic pyroxene supports the fact that this kind of rocks has a distinct peak P-T than the eclogites. For similar reasons, it is highly unlikely that blue-amphibole-bearing metacherts ever reached pressure values of eclogites (contrary to claims by Fotoohi Rad et al., 2005).

Fotoohi Rad et al. (2005) estimated the P-T conditions of these rocks at 460 °C and ~0.5 GPa for the assemblage but the presence of relict glaucophane and ferric-sodic pyroxene in some of these rocks tends to show that these rocks reached higher pressures. The absence of Fe–Mg garnet, omphacite and rutile from these rocks however pleads in favor of peak pressure largely below those of eclogites. For a MORB composition including the effect of Fe^{3+}, Diener and Powell (2012) published a pseudosection, in which a similar blueschist assemblage lies around 0.8 GPa and 450 °C and the epidote-amphibolite assemblage lies at similar or lower pressures and temperatures around 500 °C.

6. Geochronology

6.1. Method

Samples from Gazik and samples from Sulabest (the latest from the study of Angiboust et al., 2013) were carefully chosen for dating so that: (1) they bear minerals with enough K to be dated with the Ar–Ar method (i.e., mostly phengite and amphibole) and these minerals constitute a well-understood paragenesis in the rock. Selected samples were crushed and sieved; single grains of amphibole and phengite were handpicked under binocular microscope and cleaned in ultrasonic bath with acetone and distilled water. They were packaged in Al foils and irradiated for 40 h in the core of the Triga Mark II nuclear reactor of Pavia (Italia) with several aliquots of the Fish Canyon sanidine standard (28.03 ± 0.08 Ma; Jourdan and Renne, 2007) as flux monitor. Argon isotopic interferences on K and Ca were determined by irradiation of KF and CaF2 pure salts from which the following correction factors were obtained: $(^{40}Ar/^{39}Ar)K = 0.00969 \pm 0.00036$, $(^{40}Ar/^{39}Ar)K = 0.01297 \pm 0.00045$, $(^{38}Ar/^{37}Ar)Ca = 0.000727 \pm 0.000041$ and $(^{36}Ar/^{37}Ar)Ca = 0.000288 \pm 0.000016$. Argon analyses were performed at Géosciences Montpellier (France) with two analytical devices that each consist of: (a) an IR-CO_2 laser of 100 kHz used at 5–15% during 60 s, (b) a lenses system for beam focusing, (c) a steel chamber, kept at 10^{-8}–10^{-9} bar, with a drilled copper plate, (d) an inlet line for purification of gases including two Zr–Al getters, (e) a multi-collector mass spectrometer (Argus VI from Thermo-Fisher). A custom-made software controls the laser intensity, the timing of extraction/purification and the data acquisition. To measure the Ar background within the system, one blank analysis was performed every three sample analyses. ArArCalc© v2.5.2 was used for data reduction and plotting. The one-sigma errors reported on plateau, isochron and total gas ages include the error on the irradiation factor J. Atmospheric ^{40}Ar was estimated using a value of the initial $^{40}Ar/^{36}Ar$ of 295.5.

6.2. Results

The results are presented in Fig. 8 and Table 5 (14 samples) and degassing patterns are in Supplementary data S4 and S5. Ages were sorted in three categories: (1) ages given by phengite in eclogite, assumed to form during eclogitic metamorphism and possibly recrystallized during amphibolitization (Angiboust et al., 2013; e.g., Fig. 8a), (2) ages given by hornblende/barroisite in eclogite (that formed at or near the peak-T; Fig. 8b) and (3) ages of phengite and amphibole in amphibolitized blueschists (e.g., Fig. 8c). All ages are very close, around 86 ± 3 Ma, as previously shown by Bröcker et al. (2013).

All dated phengite and amphibole single grains display plateau ages for a large percentage of the argon released (from 65 to 100% of the ^{39}Ar released) with very little evidence for isotopic heterogeneities, with the exception of phengite Sum8 which contains a loosely bound excess argon component released during the first heating-steps. Inverse $^{36}Ar/^{40}Ar$ vs $^{39}Ar/^{40}Ar$ correlation plots provide intercept ages that are consistent with the plateau ages (Table 5) with initial $^{40}Ar/^{36}Ar$ ratios ranging from 291 to 310, in agreement within errors with the atmospheric value of 295.5. Intercept ages are used in the discussion below.

In Sulabest, four phengites from eclogite and amphibolitized blueschist (Fig. 8d and Supplementary data S4) have intercept ages in a narrow range from 86.6 ± 0.4 to 87.9 ± 0.6 Ma while two amphiboles from retrograded eclogites give slightly younger ages of 84.4 ± 1.2 Ma and 86.8 ± 1.0 Ma respectively. In Gazik, phengite ages from eclogites and amphibolitized blueschists show a larger spread than in Sulabest, with values between 83.5 ± 0.4 and 86.8 ± 0.4 Ma that are similar to those recorded by amphiboles from 84.0 ± 1.0 to 87.3 ± 2.7 Ma.

Therefore, the data do not indicate significantly younger ages in the most retrogressed high-pressure rocks compared to the best-preserved ones and the two studied areas appear to have followed a similar temporal evolution of metamorphic conditions. At the scale of the sample (Su-n) and the outcrop (15b21 a to d), the ^{40}Ar–^{39}Ar ages of phengite and amphibole overlap, phengite possibly being 1 Ma older than amphibole in sample Su-n. The consequences of these observations are discussed below.

7. Discussion

7.1. Relationships between structure and metamorphic grade

This study highlights the existence of two block-in-matrix complexes in the suture zone of Gazik, both containing dominantly ~1–10 m blocks of oceanic (metavolcanic and metasedimentary) rocks. In subduction contexts, three end-member mixing mechanisms are usually identified (Cloos, 1982; Festa et al., 2010; Hsü, 1968; Wakabayashi, 2011): (1) sedimentary mixing as a result from submarine gravity sliding at the trench or at oceanic core complexes, forming olistostrome in a usually sedimentary matrix, (2) tectonic mixing in highly sheared environments, purportedly at the plate interface, and (3) diapiric ascent of partly exhumed, broken-up rocks in a low-viscosity buoyant matrix.

7.1.1. Siliciclastic-matrix complex

The siliciclastic-matrix complex hosts strongly deformed and dismembered oceanic blocks: serpentinized peridotites, basalts and somewhat less abundant radiolarites. Blocks and matrix reach greenschist facies at most. Greenschist recrystallization of this complex at around ~340 °C (RSCM data; Table 4), ~400 °C ± 160 °C and 0.3–0.7 GPa (average P-T) may have occurred during shallow subduction at depths between 10 and 20 km. There is no obvious difference of metamorphism between the blocks and the matrix. This unit could be an olistostrome, formed with turbiditic currents incorporating forearc or lower plate crustal material (possibly as a result of fault bending; Ranero et al., 2003; Taira et al., 1982) or formed at the foot of an oceanic detachment; Boschi et al., 2006; this is less likely however due to the lack of gabbros). It could also originate from tectonic mixing in an accretionary wedge.

7.1.2. Serpentinite-matrix complex

The lowermost block-in-matrix complex (Figs. 2 and 3e-f) is made of serpentinite with abundant blocks of diverse lithologies corresponding to at least two different metamorphic facies: amphibolitized blueschist and mafic eclogite. Blocks are commonly m-dam large (<100 m for amphibolitized blueschists, >100 m for eclogites) and eclogites are rare, massive and poorly deformed compared to metatuffs and epidote amphibolite blocks. Metatuffs are strongly lineated and resemble those of the Upper Unit of Sulabest. Deformation is stronger in mafic blocks with abundant micas and/or metasomatic rind formation. Preserved pre-to-syn peak eclogite blocks/cores containing only rare micas may correspond to former tectonic boudins and/or much dryer protoliths.

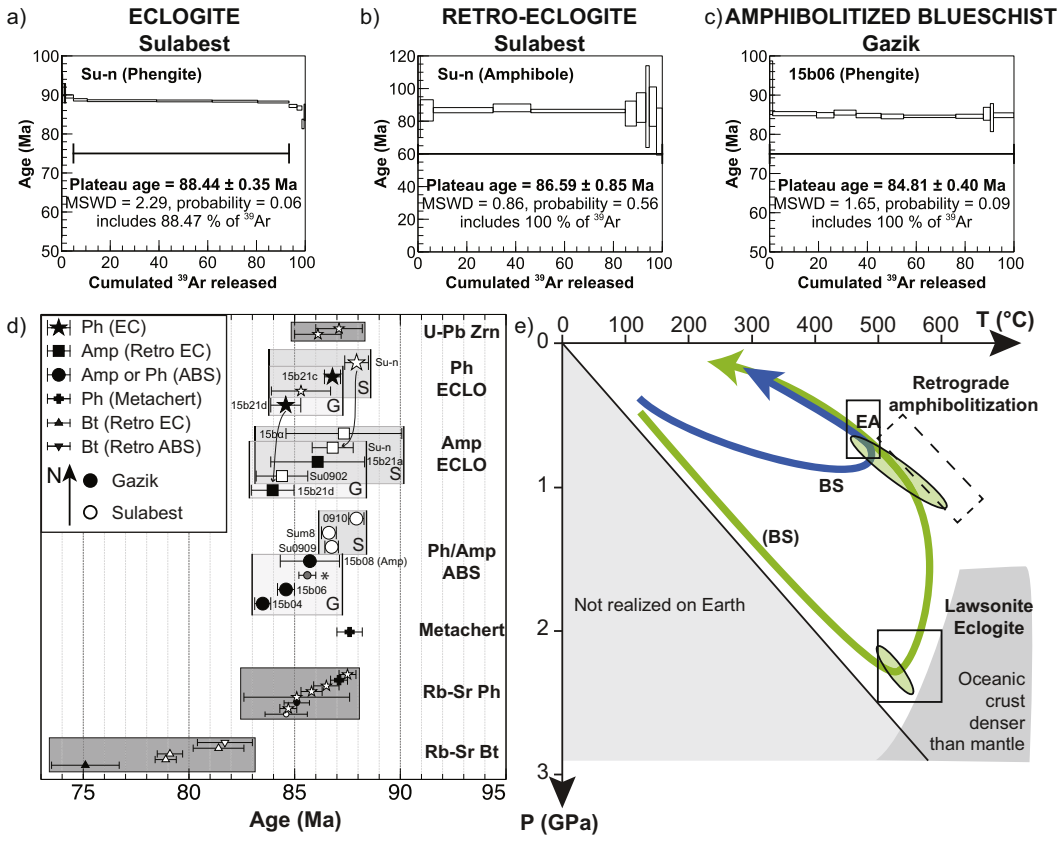

Fig. 8. a) Ar–Ar plateau age from phengite in an eclogite of Sulabest; b) Ar–Ar plateau age from retrograde amphibole in the same sample; c) Ar–Ar plateau age from phengite in an amphibolitized blueschist of Gazik; d) Summary of radiometric ages in the Sistan high-pressure rocks, sorted following age value, mineral dated, method or kind of rock and locality. G refers to Gazik, S to Sulabest. Argon-argon ages from this study are intercepts, and plateau from other studies. Arrows link phengite age and amphibole age from the same sample. Ages associated to small symbols (including all datings on metachert) are from Bröcker et al. (2013) and Kurzawa et al. (2017). * represents the locality of Gurchang between Gazik and Sulabest. ECLO = eclogite, ABS = amphibolitized blueschist; e) Synthesis of P-T paths. The green path relates to eclogite and the blue to amphibolitized blueschist. BS = blueschist, EA = epidote-amphibolite. (For interpretation of the references to colour in this figure legend, the reader is referred to the web version of this article.)

Eclogites underwent a cold prograde evolution, with blueschist facies minerals (i.e. glaucophane) preserved in garnet and lawsonite present at eclogite peak conditions, around 70–80 km. The occurrence of fresh lawsonite in Gazik makes it one of the few examples in the world where it is partly preserved during retrogression, and not only as pseudomorphs. The absence of paragonite (as part of lawsonite pseudomorphs) in the matrix may be explained by two possible reactions: formation of omphacite during prograde metamorphism or destabilization to albite during retrograde metamorphism, both of which are found in the matrix. Lawsonite stability at eclogite facies is symptomatic of rather cold subduction gradients (Tsujimori et al., 2006b; Tsujimori and Ernst, 2014), consistent with the ~7.3 °C/km prograde gradient calculated here. Cold subduction gradients are usually assigned to mature subduction and/or old oceanic plates and/or fast subduction rates (Agard et al., 2009; Ernst, 1988; Peacock, 1996; van Keken et al., 2011). Retrogression of eclogites appears almost isothermal in Gazik, and slightly colder than in Sulabest (Angiboust et al., 2013) where no lawsonite was preserved. Whether these differences relate to juxtaposition to colder or hotter slices and/or mantle wedge, and/or to slight contrasts in residence time is discussed below.

For other rocks (amphibolitized blueschist, riebeckite-bearing metachert, aegirine-augite-albite rock), estimation of P-T conditions is difficult. Preserved mineral assemblages do not enable Average P-T estimates and pseudosection calculation predicts ubiquitous clinopyroxene

Table 5
Synthesis of the argon-argon ages for each sample, detailing the fusion age, the plateau age, the intercept age, and the initial $^{40}Ar/^{36}Ar$ ratio. ABS = amphibolitized blueschist.

Sample	Lithology	Mineral	Location	Total fusion age	Plateau age	%39Ar	Intercept age	$(^{40}Ar/^{36}Ar)i$	MSWD
15b21c	Eclogite	Phengite	Gazik	86.99 ± 0.34	86.94 ± 0.33	97.25	86.79 ± 0.38	304 ± 9	0.53
15b-21d	Eclogite	Phengite	Gazik	84.39 ± 0.80	84.61 ± 0.52	100	84.58 ± 0.71	297 ± 19	0.77
Su-n	Eclogite	Phengite	Sulabest	88.37 ± 0.33	88.44 ± 0.35	88.47	87.93 ± 0.56	352 ± 50	1.13
15b21a	Eclogite	Amphibole	Gazik	88.49 ± 2.93	86.85 ± 2.04	100	86.09 ± 2.22	298 ± 3	0.43
15b-α	Eclogite	Amphibole	Gazik	91.91 ± 4.63	88.07 ± 2.65	100	87.33 ± 2.74	300 ± 4	0.11
15b21d	Eclogite	Amphibole	Gazik	83.37 ± 1.17	83.81 ± 0.94	100	83.96 ± 1.01	294 ± 4	0.66
Su0902	Eclogite	Amphibole	Sulabest	85.71 ± 1.89	84.77 ± 1.17	100	84.40 ± 1.22	301 ± 4	0.31
Su-n	Eclogite	Amphibole	Sulabest	86.84 ± 1.19	86.60 ± 0.85	100	86.80 ± 0.97	291 ± 13	0.98
15b04	ABS	Phengite	Gazik	83.73 ± 0.36	83.52 ± 0.37	78.02	83.49 ± 0.38	301 ± 5	2.15
15b06	ABS	Phengite	Gazik	84.96 ± 0.39	84.81 ± 0.40	100	84.59 ± 0.40	302 ± 4	0.58
Su0909	ABS	Phengite	Sulabest	86.79 ± 0.30	86.77 ± 0.35	100	86.61 ± 0.34	310 ± 8	3.62
Su0910	ABS	Phengite	Sulabest		87.92 ± 0.36	71.19	(Integrated)		
Sum8	ABS	Phengite	Sulabest	87.05 ± 0.33	86.82 ± 0.35	64.9	86.71 ± 0.48	304 ± 11	3.44
15b08	ABS	Amphibole	Gazik	93.40 ± 11.38	86.23 ± 1.34	100	85.72 ± 1.40	297 ± 2	0.91

stability, which is not observed. The reasons for the inadequacy of pseudosection modeling to define the P-T conditions might be: incorrect integration of ferric iron in amphibole, bulk compositions enriched in albite compared to MORB (metaspillite), or a discrepancy between the current bulk composition bulk composition at the peak due to later metasomatism (although no proof of this was observed). The absence of Fe-Mg-rich garnet, omphacite sensu stricto and lawsonite (neither fresh crystals nor pseudomorphs) in these rocks nevertheless suggest that they never experienced eclogitic P-T conditions, but instead equilibrated at blueschist-facies conditions, around 450 °C, <1.0 GPa, and were subsequently largely retrogressed to epidote-amphibolite facies, close to 500 °C, <1.0 GPa (similar to Sulabest; Angiboust et al., 2013).

A pressure/depth gap therefore exists between amphibolitized blueschists (around ~30 km) and eclogites (around 70–80 km), which coincides with the two frequency peaks in maximum depths of subducted units recovered from fossil subduction zones (Plunder et al., 2015; Fig. 9a).

7.1.3. Origin of the mélange

The origin of the serpentinite matrix is not examined in this study. One sample shows the existence of antigorite fibers in the serpentinite. In Sulabest, based on the Cr# of chromite, rare-earth elements, fluid-mobile elements and platinum-group elements, Angiboust et al. (2013) showed that Western Unit serpentinites likely originate from abyssal peridotites whereas those from the Upper and Eclogitic Units likely derive from forearc peridotites. More geochemical analyses involving isotopes (e.g., boron, Martin et al., 2016; Scambelluri and Tonarini, 2012) could help further constrain the nature of the Sistan HP serpentinites.

The outcrops of Gazik bear a number of notable differences with those of Sulabest. The serpentinite-matrix complex of Gazik gathers undistinguishably fragments of the Eclogitic and Upper Units of Sulabest (Angiboust et al., 2013), while eclogitic blocks are more numerous in Sulabest. The latter are usually less retrogressed than the Gazik ones, which show either an almost complete amphibolitization or the replacement of omphacite by ferric clinopyroxene. The Upper Unit of Sulabest is composed of continuous to hectometer-sized blocks of mafic tuffs and schists with little matrix. These rocks show assemblages very similar to the amphibolitized blueschists of Gazik, which crop out as sparse decameter-sized blocks embedded in matrix. Gazik therefore corresponds to a more dismembered equivalent of Sulabest.

Mixing and juxtaposition of the blocks in this complex could a priori tentatively be (a) sedimentary (Fig. 9a), with previously exhumed material deposited in a basin dominated by ultramafic material (i.e., serpentinites), or (b) diapiric (Fig. 9b), with exhumation of two main, serpentinite-rich buoyant units hosting small slab-derived blocks (i.e., amphibolitized blueschist and eclogite units), or result from (c) tectonic underplating and stacking of tectonic slices originating from different depths (Fig. 9c).

The first hypothesis is of particular interest in comparison with the Franciscan and Great Valley Group sedimentary serpentinite-mélanges (Wakabayashi, 2011, 2012, 2015, 2017a, 2017b). Some Californian mélanges show an ultramafic clastic matrix containing blocks of all sizes, up to a few hundred meters. The metamorphic grade of the blocks is variable, which is explained by exhumation of metamorphic slices from different depths, dismantling in sedimentary basins, and potential further resubduction (only in the Franciscan) and are usually associated with felsic volcanic rocks. Despite the absence of felsic rocks and lack of petrographic proof for resubduction of both complexes, this hypothesis cannot be completely ruled out for Gazik. Further insights on the nature of the matrix would be necessary to recognize a sedimentary mélange in Gazik, but no sedimentary character was recognized in Sulabest serpentinites. However, the sedimentary-mixing model fails to explain the exposure of eclogites below a continuous amphibolitized blueschist unit in Sulabest (and in Gazik, although it is less clear), and the absence of blocks smaller than 1 m. The formation of metasomatic rinds on eclogites needs to be explained by interaction of the blocks with serpentinite at high temperature (Moore, 1984; Ukar and Cloos, 2013). The MORB to SSZ-like geochemical signature of eclogite and

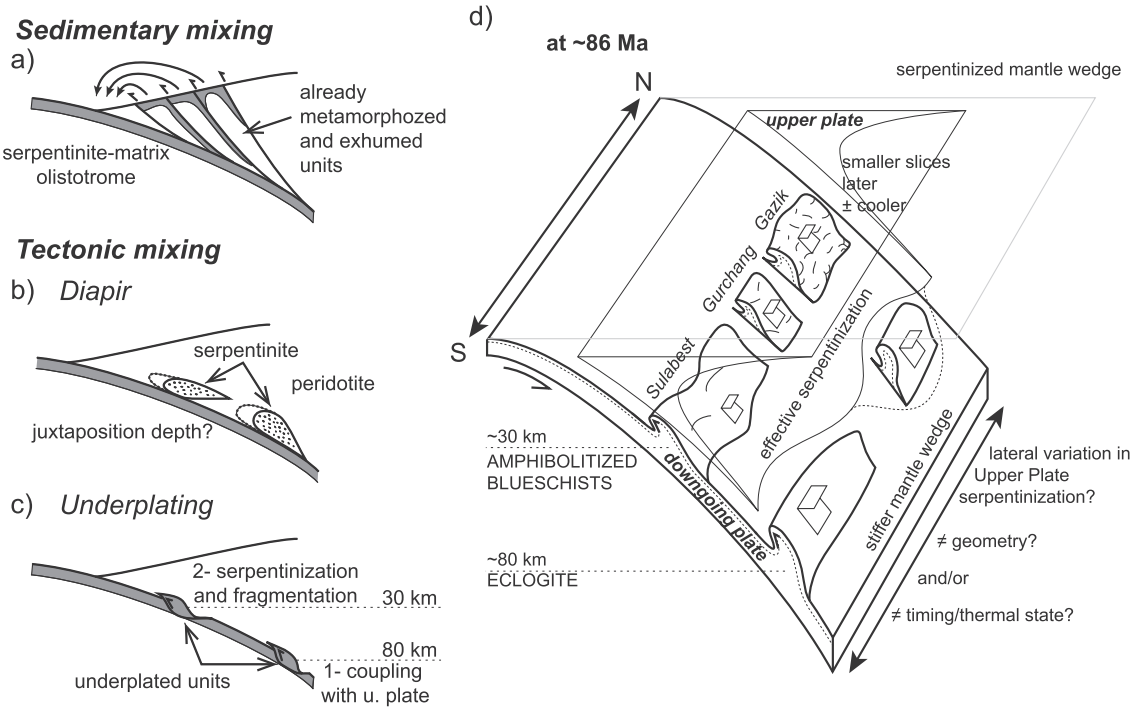

Fig. 9. a, b, c) Three different hypotheses for mixing processes. a) Sedimentary mixing hypothesis: pre-metamorphozed and exhumed olistoliths in a sedimented serpentinite; b) Serpentinite diapir to exhume and mix the blocks with serpentinite; c) Direct underplating of the blocks to a weakly serpentinized mantle wedge and subsequent fast exhumation in a low viscosity subduction channel. d) Synthesis of the processes showing the almost simultaneous underplating of eclogite and amphibolitized blueschist along the subduction interface, with the potential effect of serpentinization of the mantle wedge to explain fragmentation of the blocks in Gazik.

MORB signature of amphibolitized blueschist tuffs in Sulabest (Angiboust et al., 2013) does not give many clues on the formation mechanisms. Given all these elements, the formation of the Sistan mélange in a sedimentary context is unlikely but would need to be further examined by a detailed study of the serpentinite matrix. The second hypothesis of a diapir has also been observed in the Franciscan (Tsujimori et al., 2007) and in the Mariana forearc (Maekawa et al., 1995). Late exhumation can possibly explain the fragmentation of the outcrops in Gazik, but cannot explain the kilometer-scale tectonic continuity of the Upper Unit observed in Sulabest. In Gazik, no proofs (like consistent shear senses) argue for diapiric emplacement.

We hence favor the explanation of mélange formation by shearing at the subduction interface that can explain the continuity observed in Sulabest, the mixing of different metamorphic grades and the metamorphic rinds around eclogitic blocks. Although complex to estimate, the total thickness of the Sistan mélange (as well as other assumed tectonic mélanges, Table 1) is generally lower than the thickness of the "subduction channel" inferred from field observations (~100-1000 m; e.g., Vannucchi et al., 2012) or geophysical imaging (~1–5 km; e.g., Abers, 2005), and within the range (~500–2000 m; Ruh et al., 2015) or much lower (~10 km; Gerya, 2002) than modelled numerically.

7.2. Age interpretation and implications for Sistan

All ages of peak minerals from this study, and those of Bröcker et al. (2013), strikingly gather around 86 ± 3 Ma, whatever the dated mineral (zircon, phengite, amphibole), maximum grade of the rock (eclogite, amphibolitized blueschist) or method used (U–Pb, Ar–Ar, Rb–Sr). Only Rb–Sr ages on biotite-bearing assemblages are younger (around 80 ± 2 Ma) and are interpreted to date cooling around 300 °C (Cliff, 1985). Ages are on average older in Sulabest than in Gazik for all minerals and grades (Fig. 8d; about 1 Myr older for phengite in eclogite, 2 Myr older for amphibole in eclogite and about 3 Myr for phengite in epidote amphibolite).

Another striking feature consists in systematically older ages (1 to 2 Myrs) from phengite in eclogitic samples where both amphibole and phengite are dated (88.44 ± 0.35 Ma for phengite and 86.6 ± 0.85 Ma for amphibole in sample Su-n; 84.27 ± 0.52 Ma for phengite and 83.47 ± 0.94 Ma for amphibole in sample 15b21d). This would be consistent with the order of formation of those minerals, even though the dated phengite crystals are zoned (Supplementary S3) and record part of the prograde, peak and exhumation stages.

Using the diffusion parameters of Harrison (1981) for hornblende and Harrison et al. (2009) for muscovite in a pressure range of 5–10 kbar for which these values were calculated, the closure temperature estimated for crystals as large as 300–400 μm is in the range 550–560 °C for amphibole and 450–485 °C for white mica. It must be noticed that these temperatures are probably minimum estimates since diffusion data are lacking for the specific compositions and pressures of this study that tend to increase the retentivity for argon (Forster and Lister, 2014; Lister and Baldwin, 1996), in particular for phengite with a high Mg/Fe ratio (Scaillet et al., 1992).

Additionally, U–Pb dating on eclogite-facies stage zircons from Sulabest yield ages that are very similar to the Ar–Ar ages on phengite in eclogite (87.1 ± 1.1 Ma and 86.1 ± 1.1 Ma; Bröcker et al., 2013; Kurzawa et al., 2017; Fig. 8d).

This suggests that phengite and amphibole ages are crystallization ages and that they were not reset during exhumation, despite peak temperatures above or close to the usually expected isotopic closure temperature and pervasive fluid circulation. This behavior has been documented elsewhere (Agard et al., 2002; Berger et al., 2017; Di Vicenzo et al., 2001; Rodriguez et al., 2003) and is also expected in the case of fast cooling rates.

Based on the assumption that recorded ages are crystallization ages, eclogites are brought from their peak to the epidote-amphibolite grade in approximately 1 Myr (maximum 2.5 Myr when accounting for uncertainty), which yields exhumation rates between 15 km/Myrs (minimum estimate) to 45 km/Myrs (maximum estimate), consistent with fast exhumation in low-viscosity serpentinite channels (Gerya, 2002). These values are also similar to those for continental rocks of Dora Maira (Rubatto and Hermann, 2001), some high-pressure basal units in the Aegean (Ring and Reischmann, 2002) or ultra-high pressure eclogites from the D'Entrecasteaux Islands (Little et al., 2011).

Ages for the amphibolitized blueschists are also similar to those recorded by the eclogites. Two scenarii are therefore possible:

1) slicing from the slab and beginning of exhumation of eclogite and epidote-amphibolite at the same time, recorded as similar ages for their peak, or
2) slicing of eclogites first, then exhumation down to epidote-amphibolite facies depths, and offscrapping of amphibolitized blueschist coeval with juxtaposition of eclogites.

Age constraints are too similar to decide alone on one of these two possibilities. Structural relationships, with amphibolitized blueschist located above the eclogites here and in Sulabest (Angiboust et al., 2013), make the first scenario more likely. The first scenario is reminiscent of the coeval slicing of the subducting plate along several 100 km argued by Monié and Agard (2009).

Finally, Bröcker et al. (2013) and Kurzawa et al. (2017) dated biotite in retrograde eclogite and amphibolitized blueschists with the Rb-Sr method. Ages between 82 and 75 Ma would correspond to the last stages of exhumation at greenschist facies, occurring at slower rates (<5 km/Myr). These ages relate to pre-collisional events, since collision is dated around ~40 Ma (Mid-Eocene, Mohammadi et al., 2016a; Tirrul et al., 1983).

7.3. Insights on slicing, exhumation and mixing mechanisms along the plate interface

The siliciclastic-matrix complex extends along tens of kilometers and probably formed at or near the trench. RSCM temperature estimates around 340 °C for the matrix (Table 4), the presence of ocean-derived blocks and pervasive deformation are compatible with underplating of sediments at shallow depths in an accretionary wedge (e.g., Shimanto Belt, Kimura and Mukai, 1991; Taiwan, Beyssac et al., 2007; Western Alps, Agard et al., 2002). However, no clear high-pressure metamorphic recrystallization was observed in this unit.

In the serpentinite-matrix complex, metamorphic grade and deformation of the blocks is much more diverse, as in fact for most subduction-related serpentinite mélange-like units (Table 1). Although high-grade mafic rocks are only found in three localities (Gazik, Gurchang and Sulabest, with eclogites only exposed in Gazik and Sulabest), high-grade blocks in a serpentinite-matrix complex outcrop along 150 km in Sistan, which dismisses the possibility that detachment was very local on the subduction interface. Even more striking, the recorded age pulse for eclogites and amphibolitized blueschist (86 ± 3 Ma), 150 km apart, suggests that these rocks where detached almost coevally along the subduction zone (though at different depths) and pleads for a lithospheric scale change in boundary conditions (Klemd et al., 2011; Monié and Agard, 2009).

The fact that smaller blocks (mainly for amphibolitized blueschist) are found in Gazik than in Sulabest unit could be explained by (i) initial detachment of smaller blocks in Gazik or (ii) post-detachment dismembering, or (iii) could reflect an initially inhomogeneous seafloor structure. In all cases, detachment of material/rocks from the slab requires a strong interplate mechanical coupling, which is enhanced when effective viscosities on both sides of the subduction interface are similar, so that strain transiently localizes preferentially within the slab rather than on the plate interface (Agard et al., 2016; Kimura and Ludden, 1995).

Agard et al. (2016) showed, for example, that accretion of metamorphic soles is largely controlled by changes in the rheological parameters of the upper plate due to progressive cooling, prior to full serpentinization of the mantle wedge. Different block sizes might thus be explained by different rheologies of the downgoing and/or upper plate (e.g., contrasts in the extent of basalt hydrothermal alteration in the downgoing plate, heterogeneity of the downgoing plate or mantle wedge rheology). A more serpentinized mantle wedge would for example enable the accretion of smaller blocks only and/or at shallower depth, where the mantle wedge is colder and therefore likely more hydrated. In this case, the characteristic size of blocks (>100 m for eclogites, ~10 m for amphibolitized blueschist) may give a snapshot of the serpentinisation degree of the mantle wedge (Fig. 9d). In the case of Sistan, block size and age distribution (Gazik: smaller blocks, slightly younger; Sulabest; larger blocks, older) may indicate a higher serpentinisation degree of the mantle wedge in the North than in the South and a difference in thermal regime (whether controlled by age or geometry). We note, however, that progressive metasomatic digestion (as testified by metasomatic rinds around blocks and the presence of talc, chlorite and actinolite in the serpentinite matrix, Marschall and Schumacher, 2012) will increase dismembering and block size reduction.

8. Conclusions

Block-in-matrix complexes of the Sistan Suture Zone formed in a subduction context. While the siliciclastic-matrix complex might be the remnant of a shallowly subducted sedimentary mélange (i.e., paleo-accretionary wedge), the serpentinite-matrix complex is an example of tectonic mixing occuring at important depths in the subduction channel. This complex contains rocks that were subducted down to two contrasting depths: amphibolitized blueschists and eclogites were offscrapped respectively around depths of ~30 km and 75 km. Lawsonite eclogites are also indicative of a cold subduction environment.

Amphibolitized blueschists and eclogites record similar ages of 86 ± 3 Ma, interpreted as a broad slicing of the subducting plate and incorporation in a weakly hydrated mantle wedge. Horizontal continuity of the slicing in the slab over long distances tend to prove that slicing events might be associated to a specific rheological behavior of the subduction interface at specific conditions of pressure (Plunder et al., 2015), temperature, composition and strain-rate. In this respect, contrasting block sizes along the suture zone may reflect changes in mechanical coupling along the plate interface.

Supplementary data to this article can be found online at https://doi.org/10.1016/j.lithos.2018.04.016.

Acknowledgments

This study was essentially funded by the project “Zooming in between plates” (Marie Curie International Training Network no. 604713) to Philippe Agard. Additional support was provided by an IUF grant (Institut Universitaire de France) to Philippe Agard. We thank M. Fialin, N. Rividi (CAMPARIS), O. Boudouma (ISTeP), F. Lecœur (Géosciences Montpellier) and D. Deldicque (ENS Paris, France) for analytical support, E. Delairis and D. Devaux (ISTeP) for the preparation of thin sections and the Geological Survey of Iran for logistic support on the field. We also thank M. Soret, M. Locatelli and Tan Z. for interesting discussions. Tatsuki Tsujimori and John Wakabayashi are warmly thanked for their constructive reviews and suggestions, and Marco Scambelluri for his editorial handling leading to a significant improvement of the manuscript. This is IPGP contribution #3939.

References

Abers, G.A., 2005. Seismic low-velocity layer at the top of subducting slabs: observations, predictions, and systematics. Physics of the Earth and Planetary Interiors 149:7–29. https://doi.org/10.1016/j.pepi.2004.10.002.

Agard, P., Monié, P., Jolivet, L., Goffé, B., 2002. In situ laser probe $^{40}Ar/^{39}Ar$ dating of the Schistes Lustrés complex: implications for the exhumation of the Western Alps. Journal of Metamorphic Geology 20:599–618. https://doi.org/10.1046/j.1525-1314.2002.00391.x.

Agard, P., Monié, P., Gerber, W., Omrani, J., Molinaro, M., Meyer, B., Labrousse, L., Vrielynck, B., Jolivet, L., Yamato, P., 2006. Transient, synobduction exhumation of Zagros blueschists inferred from P-T, deformation, time, and kinematic constraints: implications for Neotethyan wedge dynamics. Journal of Geophysical Research 111: B11401. https://doi.org/10.1029/2005JB004103.

Agard, P., Yamato, P., Jolivet, L., Burov, E., 2009. Exhumation of oceanic blueschists and eclogites in subduction zones: timing and mechanisms. Earth-Science Reviews 92: 53–79. https://doi.org/10.1016/j.earscirev.2008.11.002.

Agard, P., Omrani, J., Jolivet, L., Whitechurch, H., Vrielynck, B., Spakman, W., Monié, P., Meyer, B., Wortel, M.J.R., 2011. Zagros orogeny: a subduction-dominated process. Geological Magazine 148:692–725. https://doi.org/10.1017/S001675681100046X.

Agard, P., Yamato, P., Soret, M., Prigent, C., Guillot, S., Plunder, A., Dubacq, B., Chauvet, A., Monié, P., 2016. Subduction infancy: mantle resistance to slab penetration and metamorphic sole formation controlled by plate interface rheological switches. Earth and Planetary Science Letters 451:208–220. https://doi.org/10.1016/j.epsl.2016.06.054.

Angiboust, S., Agard, P., 2010. Initial water budget: the key to detaching large volumes of eclogitized oceanic crust along the subduction channel? Lithos 120:453–474. https://doi.org/10.1016/j.lithos.2010.09.007.

Angiboust, S., Agard, P., Raimbourg, H., Yamato, P., Huet, B., 2011. Subduction interface processes recorded by eclogite-facies shear zones (Monviso, W. Alps). Lithos 127: 222–238. https://doi.org/10.1016/j.lithos.2011.09.004.

Angiboust, S., Agard, P., De Hoog, J.C.M., Omrani, J., Plunder, A., 2013. Insights on deep, accretionary subduction processes from the Sistan ophiolitic “mélange” (Eastern Iran). Lithos 156–159:139–158. https://doi.org/10.1016/j.lithos.2012.11.007.

Angiboust, S., Agard, P., Glodny, J., Omrani, J., Oncken, O., 2016. Zagros blueschists: episodic underplating and long-lived cooling of a subduction zone. Earth and Planetary Science Letters 443:48–58. https://doi.org/10.1016/j.epsl.2016.03.017.

Arjmandzadeh, R., Karimpour, M.H., Mazaheri, S.A., Santos, J.F., Medina, J.M., Homam, S.M., 2011. Sr-Nd isotope geochemistry and petrogenesis of the Chah-Shaljami granitoids (Lut Block, Eastern Iran). Journal of Asian Earth Sciences 41:283–296. https://doi.org/10.1016/j.jseaes.2011.02.014.

Babazadeh, S.A., 2013. A Note on Stratigraphic Data and Geodynamic Evolution of Sistan Suture Zone (Neo-Tethyan Margin) in Eastern Iran. Geodynamics Research International Bulletin 1.

Babazadeh, S.A., de Wever, P., 2004. Early Cretaceous radiolarian assemblages from radiolarites in the Sistan Suture (eastern Iran). Geodiversitas 26, 185–206.

Barrier, E., Vrielynck, B., Bergerat, F., Brunet, M.-F., Mosar, J., Poisson, A., Sosson, M., 2008. Palaeotectonic maps of the Middle East: Tectono-sedimentary-palinspastic maps from Late Norian to Pliocene. Atlas of 14 maps at 1/18 500 000. Publisher CGMW, Paris, France.

Bebout, G.E., Barton, M.D., 1993. Metasomatism during subduction: products and possible paths in the Catalina Schist, California. Chemical Geology 108:61–92. https://doi.org/10.1016/0009-2541(93)90318-D.

Berberian, M., Jackson, J.A., Qorashi, M., Talebian, M., Khatib, M.M., Priestley, K., 2000. The 1994 Sefidabeh earthquakes in eastern Iran: Blind thrusting and bedding-plane slip on a growing anticline, and active tectonics of the Sistan suture zone. Geophysical Journal International 142:283–299. https://doi.org/10.1046/j.1365-246X.2000.00158.x.

Berger, A., Wehrens, P., Lanari, P., Zwingmann, H., Herwegh, M., 2017. Microstructures, mineral chemistry and geochronology of white micas along a retrograde evolution: an example from the Aar massif (Central Alps, Switzerland). Tectonophysics 721: 179–195. https://doi.org/10.1016/j.tecto.2017.09.019.

Beydokhti, R.M., Karimpour, M.H., Mazaheri, S.A., Santos, J.F., Klötzli, U., 2015. U–Pb zircon geochronology, Sr–Nd geochemistry, petrogenesis and tectonic setting of Mahoor granitoid rocks (Lut Block, Eastern Iran). Journal of Asian Earth Sciences 111: 192–205. https://doi.org/10.1016/j.jseaes.2015.07.028.

Beyssac, O., Goffé, B., Chopin, C., Rouzaud, J.-N., 2002. Raman spectra of carbonaceous material in metasediments: a new geothermometer. Journal of Metamorphic Geology 20:859–871. https://doi.org/10.1046/j.1525-1314.2002.00408.x.

Beyssac, O., Simoes, M., Avouac, J.-P., Farley, K.A., Chen, Y.G., Chan, Y.C., Goffé, B., 2007. Late Cenozoic metamorphic evolution and exhumation of Taiwan. Tectonics 26. https://doi.org/10.1029/2006TC002064.

Boschi, C., Früh-Green, G.L., Delacour, A., Karson, J.A., Kelley, D.S., 2006. Mass transfer and fluid flow during detachment faulting and development of an oceanic core complex, Atlantis Massif (MAR 30° N). Geochemistry, Geophysics, Geosystems 7. https://doi.org/10.1029/2005GC001074.

Bröcker, M., Fotoohi Rad, G., Burgess, R., Theunissen, S., Paderin, I., Rodionov, N., Salimi, Z., 2013. New age constraints for the geodynamic evolution of the Sistan Suture Zone, eastern Iran. Lithos 170–171:17–34. https://doi.org/10.1016/j.lithos.2013.02.012.

Camp, V.E., Griffis, R.J., 1982. Character, genesis and tectonic setting of igneous rocks in the Sistan suture zone, eastern Iran. Lithos 15:221–239. https://doi.org/10.1016/0024-4937(82)90014-7.

Clarke, G.L., Powell, R., Fitzherbert, J.A., 2006. The lawsonite paradox: a comparison of field evidence and mineral equilibria modelling. Journal of Metamorphic Geology 24:715–725. https://doi.org/10.1111/j.1525-1314.2006.00664.x.

Cliff, R.A., 1985. Isotopic dating in metamorphic belts. Journal of the Geological Society 142:97–110. https://doi.org/10.1144/gsjgs.142.1.0097.

Cloos, M., 1982. Flow melanges: numerical modeling and geologic constraints on their origin in the Franciscan subduction complex, California. Geological Society of America Bulletin 93:330–345. https://doi.org/10.1130/0016-7606(1982)93.

Coggon, R., Holland, T.J.B., 2002. Mixing properties of phengitic micas and revised garnet-phengite thermobarometers. Journal of Metamorphic Geology 20:683–696. https://doi.org/10.1046/j.1525-1314.2002.00395.x.

Connolly, J.A.D., 1990. Multivariable phase diagrams: an algorithm based on generalized thermodynamics. American Journal of Science 290:666–718. https://doi.org/10.2475/ajs.290.6.666.

Connolly, J.A.D., 2005. Computation of phase equilibria by linear programming: a tool for geodynamic modeling and its application to subduction zone decarbonation. Earth and Planetary Science Letters 236:524–541. https://doi.org/10.1016/j.epsl.2005.04.033.

Di Vicenzo, G., Ghiribelli, B., Giorgetti, G., Palmeri, R., 2001. Evidence of a close-link between petrology and isotope records: constraints from SEM, EMP, TEM and in-situ 40Ar-39Ar laser analyses on multiple generations of white micas (Lanterman Range, Antarctica). Earth and Planetary Science Letters 192, 389–405.

Diener, J.F.A., Powell, R., 2012. Revised activity-composition models for clinopyroxene and amphibole. Journal of Metamorphic Geology 30:131–142. https://doi.org/10.1111/j.1525-1314.2011.00959.x.

Draper, G., Nagle, F., Renne, P.R., 1991. Geologic and tectonic development of the North America-Caribbean plate boundary in Hispaniola: development of the Rio San Juan Complex, northern Dominican Republic. Geological Society of America Special Papers 262:77–95. https://doi.org/10.1130/SPE262-p77.

Droop, G.T.R., 1987. A general equation for estimating Fe^{3+} concentrations in ferromagnesian silicates and oxides from microprobe analyses, using stoichiometric criteria. Mineralogical Magazine 51:431–435. https://doi.org/10.1180/minmag.1987.051.361.10.

Ernst, W.G., 1988. Tectonic history of subduction zones inferred from retrograde blueschist P-T paths. Geology 16:1081–1084. https://doi.org/10.1130/0091-7613(1988)016<1081:THOSZI>2.3.CO;2.

Farhoudi, G., Karig, D.E., 1977. Makran of Iran and Pakistan as an active arc system. Geology 5:664–668. https://doi.org/10.1130/0091-7613(1977)5<664:MOIAPA>2.0.CO;2.

Federico, L., Crispini, L., Scambelluri, M., Capponi, G., 2007. Different PT paths recorded in a tectonic melange (Voltri Massif, NW Italy): implications for the exhumation of HP rocks. Geodinamica Acta 20:3–19. https://doi.org/10.3166/ga.20.3-19.

Festa, A., Pini, G.A., Dilek, Y., Codegone, G., 2010. Mélanges and mélange-forming processes: a historical overview and new concepts. International Geology Review 52: 1040–1105. https://doi.org/10.1080/00206810903557704.

Flores, K.E., Martens, U.C., Harlow, G.E., Brueckner, H.K., Pearson, N.J., 2013. Jadeitite formed during subduction: in situ zircon geochronology constraints from two different tectonic events within the Guatemala Suture Zone. Earth and Planetary Science Letters 371–372:67–81. https://doi.org/10.1016/j.epsl.2013.04.015.

Flores, K.E., Skora, S., Martin, C., Harlow, G.E., Rodríguez, D., Baumgartner, P.O., 2015. Metamorphic history of riebeckite- and aegirine-augite-bearing high-pressure–low-temperature blocks within the Siuna Serpentinite Mélange, northeastern Nicaragua. International Geology Review 57:943–977. https://doi.org/10.1080/00206814.2015.1027747.

Forster, M.A., Lister, G.S., 2014. $^{40}Ar/^{39}Ar$ geochronology and the diffusion of ^{39}Ar in phengite-muscovite intergrowths during step-heating experiments in vacuo. Advances in $^{40}Ar/^{39}Ar$ Dating: From Archeology to Planetary Sciences. Geological Society, London, Special Publications:pp. 117–135. https://doi.org/10.1144/SP378.16.

Fotoohi Rad, G., Droop, G.T.R., Amini, S., Moazzen, M., 2005. Eclogites and blueschists of the Sistan Suture Zone, eastern Iran: a comparison of P-T histories from a subduction mélange. Lithos 84:1–24. https://doi.org/10.1016/j.lithos.2005.01.007.

Fotoohi Rad, G., Droop, G.T.R., Burgess, R., 2009. Early Cretaceous exhumation of high-pressure metamorphic rocks of the Sistan Suture Zone, eastern Iran. Geological Journal 44:104–116. https://doi.org/10.1002/gj.

Freund, R., 1970. Rotation of strike-slip faults in Sistan, Southeast Iran. Journal of Geology 78:188–200. https://doi.org/10.1086/627500.

Garcia-Casco, A., Torres-Roldán, R.L., Iturralde-Vinent, M.A., Millan, G., Nuñez Cambra, K., Lazaro, C., Rodriguez Vega, A., 2006. High pressure metamorphism of ophiolites in Cuba. Geologica Acta 4:63–88. https://doi.org/10.1344/105.000000358.

Gerya, T.V., 2002. Exhumation of high-pressure metamorphic rocks in a subduction channel: a numerical simulation. Tectonics 21. https://doi.org/10.1029/2002TC001406.

Goncalves, P., Guillot, S., Lardeaux, J.-M., Nicollet, C., Mercier De Lepinay, B., 2000. Thrusting and sinistral wrenching in a pre-Eocene HP-LT Caribbean accretionary wedge (Samana Peninsula, Dominican Republic). Geodinamica Acta 13:119–132. https://doi.org/10.1016/S0985-3111(00)00116-9.

Groppo, C., Castelli, D., 2010. Prograde P-T evolution of a lawsonite eclogite from the Monviso meta-ophiolite (Western Alps): dehydration and redox reactions during subduction of oceanic FeTi-oxide gabbro. Journal of Petrology 51:2489–2514. https://doi.org/10.1093/petrology/egq065.

Guillot, S., Hattori, K.H., Agard, P., Schwartz, S., Vidal, O., 2009. Exhumation processes in oceanic and continental subduction contexts: a review. In: Lallemand, S.E., Funiciello, F. (Eds.), Subduction Zone Geodynamics. Springer:pp. 175–205. https://doi.org/10.1007/978-3-540-87974-9.

Harlow, G.E., Hemming, S.R., Avé Lallemant, H.G., Sisson, V.B., Sorensen, S.S., 2004. Two high-pressure-low-temperature serpentinite-matrix mélange belts, Motagua fault zone, Guatemala: a record of Aptian and Maastrichtian collisions. Geology 32: 17–20. https://doi.org/10.1130/G19990.1.

Harrison, T.M., 1981. Diffusion of ^{40}Ar in hornblende. Contributions to Mineralogy and Petrology 78:324–331. https://doi.org/10.1007/BF00398927.

Harrison, T.M., Célérier, J., Aikman, A.B., Hermann, J., Heizler, M.T., 2009. Diffusion of ^{40}Ar in muscovite. Geochimica et Cosmochimica Acta 73:1039–1051. https://doi.org/10.1016/j.gca.2008.09.038.

Holland, T.J.B., Powell, R., 1990. An enlarged and updated internally consistent thermodynamic dataset with uncertainties and correlations: the system K_2O-Na_2O-CaO-MgO-MnO-FeO-Fe_2O_3-Al_2O_3-TiO_2-SiO_2-C-H_2-O_2. Journal of Metamorphic Geology 8: 89–124. https://doi.org/10.1111/j.1525-1314.1985.tb00325.x.

Holland, T.J.B., Powell, R., 1998. An internally consistent thermodynamic data set for phases of petrological interest. Journal of Metamorphic Geology 16:309–343. https://doi.org/10.1111/j.1525-1314.1998.00140.x.

Holland, T.J.B., Baker, J., Powell, R., 1998. Mixing properties and activity-composition relationships of chlorites in the system MgO-FeO-Al_2O_3-SiO_2-H_2O. European Journal of Mineralogy 10:395–406. https://doi.org/10.1127/ejm/10/3/0395.

Hsü, K.J., 1968. Principles of mélanges and their bearing on the Franciscan-Knoxville paradox. Geological Society of America Bulletin 79:1063–1074. https://doi.org/10.1130/0016-7606(1968)79[1063:POMATB]2.0.CO;2.

Jentzer, M., Fournier, M., Agard, P., Omrani, J., Khatib, M.M., 2017. Neogene to present paleostress field in Eastern Iran (Sistan belt) and implications for regional geodynamics. Tectonics 36.

Jourdan, F., Renne, P.R., 2007. Age calibration of the Fish Canyon sanidine $^{40}Ar/^{39}Ar$ dating standard using primary K-Ar standards. Geochimica et Cosmochimica Acta 71: 387–402. https://doi.org/10.1016/j.gca.2006.09.002.

Kimura, G., Ludden, J., 1995. Peeling oceanic crust in subduction zones. Geology 23: 217–220. https://doi.org/10.1130/0091-7613(1995)023<0217.

Kimura, G., Mukai, A., 1991. Underplated units in an accretionary complex: mélange of the Shimanto Belt of Eastern Shikoku, Southwest Japan. Tectonics 10, 31–50.

Klemd, R., John, T., Scherer, E.E., Rondenay, S., Gao, J., 2011. Changes in dip of subducted slabs at depth: petrological and geochronological evidence from HP–UHP rocks (Tianshan, NW-China). Earth and Planetary Science Letters 310:9–20. https://doi.org/10.1016/j.epsl.2011.07.022.

Krebs, M., Schertl, H.-P., Maresch, W.V., Draper, G., 2011. Mass flow in serpentinite-hosted subduction channels: P–T–t path patterns of metamorphic blocks in the Rio San Juan mélange (Dominican Republic). Journal of Asian Earth Sciences 42:569–595. https://doi.org/10.1016/j.jseaes.2011.01.011.

Kurzawa, T., Bröcker, M., Fotoohi Rad, G., Berndt, J., Lisker, F., 2017. Cretaceous high-pressure metamorphism and low pressure overprint in the Sistan Suture Zone, eastern Iran: additional temperature estimates for eclogites, geological significance of U–Pb zircon ages and Rb–Sr constraints on the timing of exhumation. Journal of Asian Earth Sciences 147:332–344. https://doi.org/10.1016/j.jseaes.2017.07.051.

Lahfid, A., Beyssac, O., Deville, E., Negro, F., Chopin, C., Goffé, B., 2010. Evolution of the Raman spectrum of carbonaceous material in low-grade metasediments of the Glarus Alps (Switzerland). Terra Nova 22:354–360. https://doi.org/10.1111/j.1365-3121.2010.00956.x.

Leake, B.E., Wolley, A.R., Arps, C.E.S., Birch, W.D., Gilbert, M.C., Grice, J.D., Hawthorne, F.C., Kato, A., Kisch, H., Krivovichev, V.G., Linthout, K., Laird, J., Mandarino, J.A., Maresch, W.V., Nickel, E.H., Rock, N.M.S., Schumacher, J.C., Smith, D.C., Stephenson, N.C.N., Ungaretti, L., Whittaker, E.J.W., Youzhi, G., 1997. Nomenclature of amphiboles: report of the subcommittee on amphiboles of the International Mineralogical Association, Commission on New Minerals and Mineral Names. The Canadian Mineralogist 35: 219–246. https://doi.org/10.1127/ejm/9/3/0623.

Lister, G.S., Baldwin, S.L., 1996. Modelling the effect of arbitrary P-T-t histories on argon diffusion in minerals using the Mac Argon program for the Apple Macintosh. Tectonophysics 253:83–109. https://doi.org/10.1016/0040-1951(95)00059-3.

Little, T.A., Hacker, B.R., Gordon, S.M., Baldwin, S.L., Fitzgerald, P.G., Ellis, S., Korchinski, M., 2011. Diapiric exhumation of Earth's youngest (UHP) eclogites in the gneiss domes of the D'Entrecasteaux Islands, Papua New Guinea. Tectonophysics 510:39–68. https://doi.org/10.1016/j.tecto.2011.06.006.

Maekawa, H., Fryer, P., Ozaki, A., 1995. Incipient blueschist-facies metamorphism in the active subduction zone beneath the Mariana forearc. Active Margins and Marginal Basins of the Western Pacific:pp. 281–289 https://doi.org/10.1029/GM088p0281.

Marschall, H.R., Schumacher, J.C., 2012. Arc magmas sourced from mélange diapirs in subduction zones. Nature Geoscience 5:862–867. https://doi.org/10.1038/ngeo1634.

Martens, U.C., Tsujimori, T., Liou, J.G., 2017. Eclogite varieties and petrotectonic evolution of the northern Guatemala Suture Complex. International Geology Review 59: 721–740. https://doi.org/10.1080/00206814.2016.1245592.

Martin, C., Flores, K.E., Harlow, G.E., 2016. Boron isotopic discrimination for subduction-related serpentinites. Geology 44:899–902. https://doi.org/10.1130/G38102.1.

Mattei, M., Cifelli, F., Muttoni, G., Rashid, H., 2015. Post-Cimmerian (Jurassic-Cenozoic) paleogeography and vertical axis tectonic rotations of Central Iran and the Alborz Mountains. Journal of Asian Earth Sciences 102:92–101. https://doi.org/10.1016/j.jseaes.2014.09.038.

Maurizot, P., 1980. Explanatory Text of the Shahrakht Quadrangle Map 1:250,000.

Moeinzadeh, H., 2015. Hyperspectral mapping of Iranian east ophiolite mélanges using neural network classification method. Arabian Journal of Geosciences 8:2169–2178. https://doi.org/10.1007/s12517-014-1333-y.

Mohammadi, A., Burg, J.-P., Bouilhol, P., Ruh, J.B., 2016a. U–Pb geochronology and geochemistry of Zahedan and Shah Kuh plutons, southeast Iran: Implication for closure of the South Sistan suture zone. Lithos 248–251:293–308. https://doi.org/10.1016/j.lithos.2016.02.003.

Mohammadi, A., Burg, J.-P., Winkler, W., Ruh, J.B., von Quadt, A., 2016b. Detrital zircon and provenance analysis of Late Cretaceous-Miocene onshore Iranian Makran strata: implications for the tectonic setting. Bulletin Geological Society of America 128: 1481–1499. https://doi.org/10.1130/B31361.1.

Monié, P., Agard, P., 2009. Coeval blueschist exhumation along thousands of kilometers: Implications for subduction channel processes. Geochemistry, Geophysics, Geosystems 10. https://doi.org/10.1029/2009GC002428.

Moore, D.E., 1984. Metamorphic history of a high-grade blueschist exotic block from the Franciscan complex, California. Journal of Petrology 25:126–150. https://doi.org/10.1093/petrology/25.1.126.

Nâini, A., Guillou, Y., Maurizot, P., Vaslet, D., de la Villéon, H., Hottin, A.M., Andreieff, P., Ancelin, J., Dânesfâleh, M., Sâjedi, T., 1981. 1:100000 map of the Âhangarân quadrangle. Geol. Map Iran 1 100 000 Ser. Sheet 8056.

Pabst, S., Zack, T., Savov, I.P., Ludwig, T., Rost, D., Tonarini, S., Vicenzi, E.P., 2012. The fate of subducted oceanic slabs in the shallow mantle: insights from boron isotopes and light element composition of metasomatized blueschists from the Mariana forearc. Lithos 132:162–179. https://doi.org/10.1016/j.lithos.2011.11.010.

Pang, K.N., Chung, S.L., Zarrinkoub, M.H., Khatib, M.M., Mohammadi, S.S., Chiu, H.Y., Chu, C.H., Lee, H.Y., Lo, C.H., 2013. Eocene-Oligocene post-collisional magmatism in the Lut-Sistan region, eastern Iran: magma genesis and tectonic implications. Lithos 180–181:234–251. https://doi.org/10.1016/j.lithos.2013.05.009.

Parkinson, C.D., 1996. The origin and significance of metamorphosed tectonic blocks in melanges: evidenc from Sulawesi, Indonesia. Terra Nova 8:312–323. https://doi.org/10.1111/j.1365-3121.1996.tb00564.x.

Peacock, S.M., 1996. Thermal and petrologic structure of subduction zones. Subduction: Top to Bottom:pp. 119–133. https://doi.org/10.1029/GM096p0119.

Platt, J.P., 1975. Metamorphic and deformational processes in the Franciscan Complex, California: some insights from the Catalina Schist terrane. Bulletin Geological Society of America 86:1337–1347. https://doi.org/10.1130/0016-7606(1975)86<1337:MADPIT>2.0.CO;2.

Plunder, A., Agard, P., Chopin, C., Pourteau, A., Okay, A.I., 2015. Accretion, underplating and exhumation along a subduction interface: from subduction initiation to continental subduction (Tavsanli zone, W. Turkey). Lithos 226:233–254. https://doi.org/10.1016/j.lithos.2015.01.007.

Powell, R., Holland, T.J.B., 1994. Optimal geothermometry and geobarometry. American Mineralogist 79:120–133. https://doi.org/10.1111/j.1365-3121.1996.tb00564.x.

Ranero, C.R., Phipps Morgan, J., McIntosh, K., Reichert, C., 2003. Bending-related faulting and mantle serpentinization at the Middle America trench. Nature 425:367–373. https://doi.org/10.1038/nature01961.

Ring, U., Reischmann, T., 2002. The weak and superfast Cretan detachment, Greece: exhumation at subduction rates in extruding wedges. Journal of the Geological Society of London 159:225–228. https://doi.org/10.1144/0016-764901-150.

Rodriguez, J., Cosca, M.A., Gil Ibarguchi, J.I., Dallmeyer, R.D., 2003. Strain partitioning and preservation of $^{40}Ar/^{39}Ar$ ages during Variscan exhumation of a subducted crust (Malpica–Tui complex, NW Spain). Lithos 70:11–139. https://doi.org/10.1016/S0024-4937(03)00095-1.

Rubatto, D., Hermann, J., 2001. Exhumation as fast as subduction? Geology 29:3–6. https://doi.org/10.1130/0091-7613(2001)?029<0003:EAFAS>?2.0.CO.

Ruh, J.B., Le Pourhiet, L., Agard, P., Burov, E., Gerya, T.V., 2015. Tectonic slicing of subducting oceanic crust along plate interfaces: numerical modeling. Geochemistry, Geophysics, Geosystems 16:3505–3531. https://doi.org/10.1002/2014GC005684.Key.

Saccani, E., Delavari, M., Beccaluva, L., Amini, S., 2010. Petrological and geochemical constraints on the origin of the Nehbandan ophiolitic complex (eastern Iran): implication for the evolution of the Sistan Ocean. Lithos 117:209–228. https://doi.org/10.1016/j.lithos.2010.02.016.

Saccani, E., Delavari, M., Dolati, A., Marroni, M., Pandolfi, L., Chiari, M., Barbero, E., 2017. New insights into the geodynamics of Neo-Tethys in the Makran area: evidence from age and petrology of ophiolites from the Coloured Mélange Complex (SE Iran). Gondwana Research. https://doi.org/10.1016/j.gr.2017.07.013.

Sadeghian, M., Bouchez, J.L., Nédélec, A., Siqueira, R., Valizadeh, M.V., 2005. The granite pluton of Zahedan (SE Iran): a petrological and magnetic fabric study of a syntectonic sill emplaced in a transtensional setting. Journal of Asian Earth Sciences 25:301–327. https://doi.org/10.1016/j.jseaes.2004.03.001.

Scaillet, S., Feraud, G., Ballèvre, M., Amouric, M., 1992. Mg/Fe and [(Mg,Fe)Si-Al_2] compositional control on argon behaviour in high-pressure white micas: a $^{40}Ar/^{39}Ar$ continuous laser-probe study from the Dora-Maira nappe of the internal western Alps, Italy. Geochimica et Cosmochimica Acta 56:2851–2872. https://doi.org/10.1016/0016-7037(92)90364-O.

Scambelluri, M., Tonarini, S., 2012. Boron isotope evidence for shallow fluid transfer across subduction zones by serpentinized mantle. Geology 40:907–910. https://doi.org/10.1130/G33233.1.

Sorensen, S.S., Barton, M.D., 1987. Metasomatism and partial melting in a subduction complex: Catalina schist, southern California. Geology 15:115–118. https://doi.org/10.1130/0091-7613(1987)15<115:MAPMIA>2.0.CO;2.

Stampfli, G.M., Borel, G.D., 2002. A plate tectonic model for the Paleozoic and Mesozoic constrained by dynamic plate boundaries and restored synthetic ocean isochrons. Earth and Planetary Science Letters 196:17–33. https://doi.org/10.1016/S0012-821X(01)00588-X.

Stöcklin, J., 1968. Structural history and tectonics of Iran: a review. American Association of Petroleum Geologists Bulletin 52, 1229–1258.

Taira, A., Okada, H., Whitaker, J.H.M., Smith, A.J., 1982. The Shimanto Belt of Japan: Cretaceous-lower Miocene active-margin sedimentation. Geological Society of London, Special Publication 10:5–26. https://doi.org/10.1144/GSL.SP.1982.010.01.01.

Tirrul, R., Bell, I.R., Griffis, R.J., Camp, V.E., 1983. The Sistan suture zone of eastern Iran. Geological Society of America Bulletin 94:134–150. https://doi.org/10.1130/0016-7606(1983)94<134.

Tsujimori, T., Ernst, W.G., 2014. Lawsonite blueschists and lawsonite eclogites as proxies for palaeo-subduction zone processes: a review. Journal of Metamorphic Geology 32:437–454. https://doi.org/10.1111/jmg.12057.

Tsujimori, T., Sisson, V.B., Liou, J.G., Harlow, G.E., Sorensen, S.S., 2006a. Petrologic characterization of Guatemalan lawsonite eclogite; eclogitization of subducted oceanic crust in a cold subduction zone. Special Paper of the Geological Society of America 403:147–168. https://doi.org/10.1130/2006.2403(09).

Tsujimori, T., Sisson, V.B., Liou, J.G., Harlow, G.E., Sorensen, S.S., 2006b. Very-low-temperature record of the subduction process: a review of worldwide lawsonite eclogites. Lithos 92:609–624. https://doi.org/10.1016/j.lithos.2006.03.054.

Tsujimori, T., Liou, J.G., Coleman, R.G., 2007. Finding of high-grade tectonic blocks from the New Idria serpentinite body, Diablo Range, California: petrologic constraints on the tectonic evolution of an active serpentinite diapir. Geological Society of America Special Papers 419:67–80. https://doi.org/10.1130/2007.2419(03).

Ukar, E., Cloos, M., 2013. Actinolitic rinds on low-T mafic blueschist blocks in the Franciscan shale-matrix mélange near San Simeon: implications for metasomatism and tectonic history. Earth and Planetary Science Letters 377–378:155–168. https://doi.org/10.1016/j.epsl.2013.06.038.

van Keken, P.E., Hacker, B.R., Syracuse, E.M., Abers, G.A., 2011. Subduction factory: 4. Depth-dependent flux of H_2O from subducting slabs worldwide. Journal of Geophysical Research 116:B01401. https://doi.org/10.1029/2010JB007922.

Vannucchi, P., Sage, F., Phipps Morgan, J., Remitti, F., Collot, J.-Y., 2012. Toward a dynamic concept of the subduction channel at erosive convergent margins with implications for interplate material transfer. Geochemistry, Geophysics, Geosystems 13. https://doi.org/10.1029/2011GC003846.

Wakabayashi, J., 2011. Mélanges of the Franciscan Complex, California: diverse structural settings, evidence for sedimentary mixing, and their connection to subduction processes. Geological Society of America Special Papers 480:117–141. https://doi.org/10.1130/2011.2480(05).

Wakabayashi, J., 2012. Subducted sedimentary serpentinite mélanges: record of multiple burial–exhumation cycles and subduction erosion. Tectonophysics 568–569:230–247. https://doi.org/10.1016/j.tecto.2011.11.006.

Wakabayashi, J., 2015. Anatomy of a subduction complex: architecture of the Franciscan Complex, California, at multiple length and time scales. International Geology Review 57:37–41. https://doi.org/10.1080/00206814.2014.998728.

Wakabayashi, J., 2017a. Sedimentary serpentinite and chaotic units of the lower Great Valley Group forearc basin deposits, California: updates on distribution and characteristics. International Geology Review 59:599–620. https://doi.org/10.1080/00206814.2016.1219679.

Wakabayashi, J., 2017b. Serpentinites and serpentinites: variety of origins and emplacement mechanisms of serpentinite bodies in the California Cordillera. Island Arc 26. https://doi.org/10.1111/iar.12205.

White, R.W., Powell, R., Holland, T.J.B., 2007. Progress relating to calculation of partial melting equilibria for metapelites. Journal of Metamorphic Geology 25:511–527. https://doi.org/10.1111/j.1525-1314.2007.00711.x.

Zarrinkoub, M.H., Pang, K.N., Chung, S.L., Khatib, M.M., Mohammadi, S.S., Chiu, H.Y., Lee, H.Y., 2012. Zircon U-Pb age and geochemical constraints on the origin of the Birjand ophiolite, Sistan suture zone, eastern Iran. Lithos 154:392–405. https://doi.org/10.1016/j.lithos.2012.08.007.